



Large Engine Technology (LET) Short Haul Civil Tiltrotor Contingency Power Materials Knowledge and Lifing Methodologies

Samuel D. Spring
GE Aircraft Engines, Lynn, Massachusetts

The NASA STI Program Office . . . in Profile

Since its founding, NASA has been dedicated to the advancement of aeronautics and space science. The NASA Scientific and Technical Information (STI) Program Office plays a key part in helping NASA maintain this important role.

The NASA STI Program Office is operated by Langley Research Center, the Lead Center for NASA's scientific and technical information. The NASA STI Program Office provides access to the NASA STI Database, the largest collection of aeronautical and space science STI in the world. The Program Office is also NASA's institutional mechanism for disseminating the results of its research and development activities. These results are published by NASA in the NASA STI Report Series, which includes the following report types:

- **TECHNICAL PUBLICATION.** Reports of completed research or a major significant phase of research that present the results of NASA programs and include extensive data or theoretical analysis. Includes compilations of significant scientific and technical data and information deemed to be of continuing reference value. NASA's counterpart of peer-reviewed formal professional papers but has less stringent limitations on manuscript length and extent of graphic presentations.
- **TECHNICAL MEMORANDUM.** Scientific and technical findings that are preliminary or of specialized interest, e.g., quick release reports, working papers, and bibliographies that contain minimal annotation. Does not contain extensive analysis.
- **CONTRACTOR REPORT.** Scientific and technical findings by NASA-sponsored contractors and grantees.

- **CONFERENCE PUBLICATION.** Collected papers from scientific and technical conferences, symposia, seminars, or other meetings sponsored or cosponsored by NASA.
- **SPECIAL PUBLICATION.** Scientific, technical, or historical information from NASA programs, projects, and missions, often concerned with subjects having substantial public interest.
- **TECHNICAL TRANSLATION.** English-language translations of foreign scientific and technical material pertinent to NASA's mission.

Specialized services that complement the STI Program Office's diverse offerings include creating custom thesauri, building customized databases, organizing and publishing research results . . . even providing videos.

For more information about the NASA STI Program Office, see the following:

- Access the NASA STI Program Home Page at <http://www.sti.nasa.gov>
- E-mail your question via the Internet to help@sti.nasa.gov
- Fax your question to the NASA Access Help Desk at 301-621-0134
- Telephone the NASA Access Help Desk at 301-621-0390
- Write to:
NASA Access Help Desk
NASA Center for Aerospace Information
7121 Standard Drive
Hanover, MD 21076



Large Engine Technology (LET) Short Haul Civil Tiltrotor Contingency Power Materials Knowledge and Lifing Methodologies

Samuel D. Spring
GE Aircraft Engines, Lynn, Massachusetts

Prepared under Contract NAS3-26617

National Aeronautics and
Space Administration

Glenn Research Center

Document History

This research was originally published internally as AST036 in July 2000,
and was not subjected to editorial review.

Trade names or manufacturers' names are used in this report for identification only. This usage does not constitute an official endorsement, either expressed or implied, by the National Aeronautics and Space Administration.

Available from

NASA Center for Aerospace Information
7121 Standard Drive
Hanover, MD 21076

National Technical Information Service
5285 Port Royal Road
Springfield, VA 22100

Available electronically at <http://gltrs.grc.nasa.gov>

TABLE OF CONTENTS

Section	Page
1.0 Introduction	1
1.1 Objective	1
1.2 Phase I Study Results	1
1.3 Phase II Program	2
1.3.1 Phase II Material Test Program	2
1.3.2 Life Prediction Methodology	4
2.0 Mechanical Test Program	6
2.1 Introduction	6
2.2 Approach	7
2.3 Tensile Relaxation Test Procedure	8
2.4 Tensile Relaxation Test Results	10
2.5 Creep Tests	11
2.6 Mixed Creep–Plasticity Tests	12
2.7 Simulated OEI Event	12
2.8 Results and Conclusions	12
3.0 Single Crystal Models	14
3.1 Introduction	14
3.2 Review of Relevant Material Characteristics	14
3.3 Modeling Approach	15
3.4 Recommendations for Future Work	15
4.0 GVIPS Model for DS Material	17
4.1 Model Basics	17
4.2 Model Considerations	17
4.3 Model Predictions	17
5.0 References	22
Appendix A Single Crystal Materials	25
A.1 Introduction	25
A.2 Materials with Elastic Cubic Symmetry	25
A.3 Inelastic Slip Mechanisms	28
A.4 Lattice Rotation and Creep	33
A.5 Kinematic Equations for Crystallographic Slip	35
A.6 Modeling of Single Crystal Alloys	39
A.7 Material Parameters and Calculated Results	42
Appendix B Evaluation of the GVIPS Constitutive Model and COMPARE Code	47
B.1 Introduction	47
B.2 The GVIPS Model	47
B.3 Evaluation of a Uniaxial GVIPS Equation	48
B.4 Evaluation of the Material Parameters	50
B.5 A Model for Tertiary Creep	52
B.6 Overall Evaluation of the GVIPS/COMPARE System	52

TABLE OF CONTENTS (Continued)

Section

Appendix C	Modeling Approach	55
C.1	Characteristics of Modern Constitutive Equations	55

1.0 INTRODUCTION

1.1 OBJECTIVE

The original objective of this program was to perform studies that would develop enhanced contingency power capability for turboshaft engines in tiltrotor applications. The intent was that the result of these studies would yield a design definition or methodology that could lead to a reduction in both engine size and the cost required to hover safely on one engine thereby improving aircraft economics. The measure to be used in these studies was: Reduced aircraft operating cost versus conventional turboshaft.

1.2 PHASE I STUDY RESULTS

Phase I of this program was completed and reported on NASA Contract Number NAS3-26617, Task Order #48. In phase I, a study plan was put together as follows:

- 1.) Establish baseline engine and aircraft
- 2.) Identify and screen contingency power and enhancing concepts
- 3.) Select best concepts, define, and evaluate concepts versus baseline
- 4.) Identify key technologies and development plan.

From this plan, the following two concepts were selected for further definition and evaluation:

- 1.) Throttle push with cooled power turbine
- 2.) Modulated high pressure and power turbine cooling air.

The results of these studies were as follows:

- Modulated cooling and throttle push concepts yield biggest payoff and have highest probability of success.
 - 3 to 4% improvement in DOC \Rightarrow +30% to +80% in operating profits.
- For the studied range of compressor pressure ratios (1.25 to 1.4), both concepts have similar payoff.
 - Best concept for application depends on specific engine configuration and mission requirements.

The study was performed using standard lifing methodologies which can't accurately model short duration material properties. From this, it was concluded that a key technology for most contingency power concepts is the development of a life prediction methodology for high power, short duration ratings. It is believed that better modeling could yield further DOC improvements and lower development program cost and risk and would allow existing engines to be rerated for higher contingency power. This formed the basis for the phase II of this program which is reported on here.

1.3 PHASE II PROGRAM

Phase II of this program was aimed at improving materials knowledge and lifting methodologies. The goals of the program were as follows:

- 1.) Conduct testing to characterize material behavior at these conditions
- 2.) Develop a computational life prediction methodology integrating the obtained material data.

1.3.1 Phase II - Material Test Program

Material Description

Utilizes two advanced alloys:

- 1.) Rene' 142 Directionally Solidified Alloy (DS) - prime HPTB material used in many GEAE applications including CF6, CFM56, CF34, CT7, and GE90
- 2.) Rene' N6 Single Crystal Alloy (SX) - 3rd generation SX alloy also in production.

Both alloys are backed by a large mechanical and physical property data base that is practically truncated at the contingency power setting condition.

Testing Philosophy

- 1.) Follow test approach of Arnold, Castelli and Saleeb to generate GVIPS materials constants, which was a challenge for the commercial test vendors
- 2.) Test in the longitudinal orientation - principal stress direction
- 3.) Use time and temperature frame consistent with OEI event
- 4.) Use closed loop computer controlled test machines "record all the data"
- 5.) Simulate an OEI event in test environment

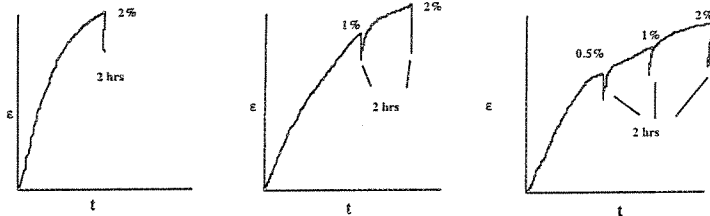
Figure 1-1 shows the Phase II test matrix and Figure 1-2 shows the validation tests.

Stress Relaxation/Tensile

Temperature 1600°F-2300°F

Strain Rate 1.0E-06 - 1.00E-01/s

122 tests

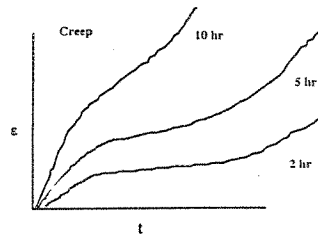


Constant Stress Creep

Temperature 1600°F-2300°F

Times 1- 24 hrs plus some longer

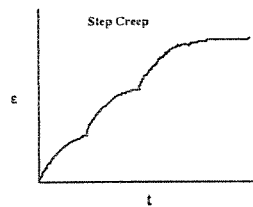
50 tests



Stepped Stress Creep

Temperature 1600°F-2300°F

22 total

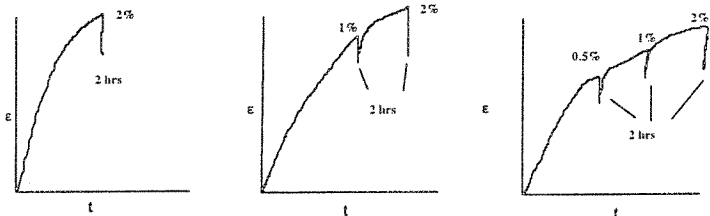


Stress Relaxation/Tensile

Temperature 1600°F-2300°F

Strain Rate 1.0E-06 - 1.00E-01/s

122 tests

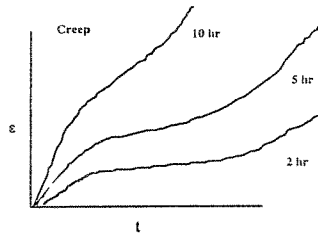


Constant Stress Creep

Temperature 1600°F-2300°F

Times 1- 24 hrs plus some longer

50 tests



Stepped Stress Creep

Temperature 1600°F-2300°F

22 total

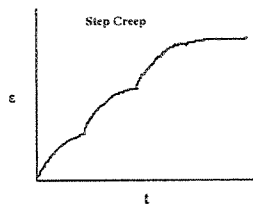
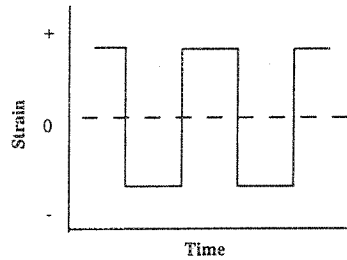


Figure 1-1. Phase II Test Matrix.

SPLCF

Temperature 1800°F-2200°F
16 tests



Cyclic Temperature Creep - Simulates the OEI Event

Temperature 2000°F - 2200°F
12 tests

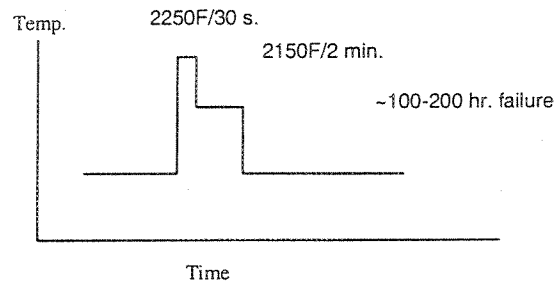
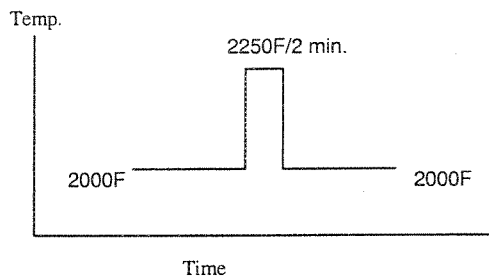


Figure 1-2. Validation Tests.

1.3.2 Life Prediction Methodology

Locations of typical turbine blade life limiting mechanisms are shown in Figure 1-3. Currently, turbine blades are lifed for Stress Rupture (creep) or for Low Cycle Fatigue (LCF). Tensile yield is evaluated for engine over-temperature certification. Turbine blades are assumed “damaged” after a single over-temperature event. No attempt is made to quantify over-temperature damage with respect to stress rupture or LCF life limits, which is a practice that introduces an unnecessary amount of conservatism into the blade design. In addition, the current blade lifing approach de-couples inelastic strain as outlined below:

Current Approach

$$\epsilon^{\text{total}} = \epsilon^{\text{elastic}} + \epsilon^{\text{plastic}} + \epsilon^{\text{creep}}$$

Time Independent
Time Dependent

Time independent analysis assumes:

Inelastic Strain = Plastic Strain (Tensile Yield)

$$\epsilon^{\text{total}} = \epsilon^{\text{elastic}} + \epsilon^{\text{plastic}}$$

Design requirement: survive an over-temperature event without tensile yield leading to component failure (short time).

Time dependent analysis assumes:

Inelastic Strain = Creep Strain (Stress Rupture)

$$\epsilon^{\text{total}} = \epsilon^{\text{elastic}} + \epsilon^{\text{creep}}$$

Design requirement: endure application mission life without tertiary creep (onset of voiding) in component (long time).

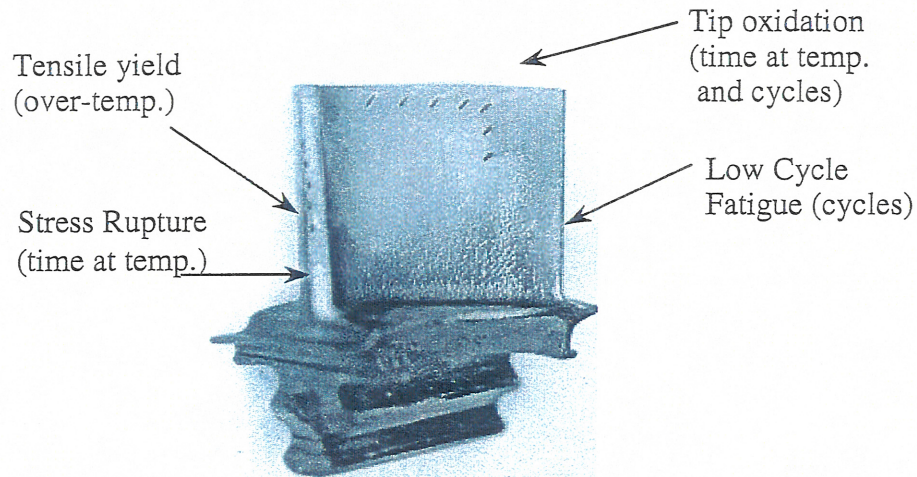


Figure 1.3. Turbine Blade Life Limiting Mechanisms.

The new life prediction methodology developed in phase II integrates the material data from the test program with a unified approach that couples inelastic strains as described below:

Unified Approach

$$\epsilon^{\text{total}} = \epsilon^{\text{elastic}} + \epsilon^{\text{plastic}} + \epsilon^{\text{creep}}$$

$$\epsilon^{\text{total}} = \epsilon^{\text{elastic}} + \epsilon^{\text{inelastic}}$$

A blue arrow points from the $\epsilon^{\text{plastic}} + \epsilon^{\text{creep}}$ term in the equation above to the $\epsilon^{\text{inelastic}}$ term in this equation.

Modeling material response to over-temperature events will allow prediction of impact on residual stress rupture life.

- Several unified constitutive models are available. Models evaluated in this study are:
 - Generalized Viscoplasticity with Potential Structure (GVIPS), Arnold and Saleeb
 - Single Crystal, Stouffer, Dame, and Sheh
 - Both Models Developed Under NASA Funding

Details of the test program and the life prediction methodology are discussed in the following sections.

2.0 MECHANICAL TEST PROGRAM

2.1 INTRODUCTION

The ability to design advanced turbine components critically hinges on the description of real material behavior. Since turbine blades and nozzles experience wide spectrums of temperature and loading, predicting component response requires design methodologies which vary from the classical approaches of independent plasticity and creep. Additionally, in order to attain optimum strength these material descriptions must address the anisotropy inherent in modern Ni-base superalloy components, since these usually have either a directionally solidified (DS) or single crystal (SX) microstructure.

The problems cited have resulted in considerable interest in the "state variable" approach to material constitutive behavior. This approach has developed from a synthesis of modeling, physical metallurgy and experiment over the last two decades². The historical development of these state variable models can be traced in many references³⁻¹⁴. A multitude of models exist and several state variable-based models have been applied to Ni-base superalloys¹⁵⁻²⁶; however, two models are of particular interest to the OEI Tiltrotor initiative. These are the Generalized Viscoplasticity and Potential Structure (GVIPS) approach of Arnold, Saleeb and Castelli²²⁻²⁶ and the Single Crystal models of Stouffer et al¹⁷⁻¹⁹. Potentially, the GVIPS model can be applied to both DS and SX materials while the Single Crystal model is unique to the single crystal deformation restraints. Particular attention has been made in the GVIPS approach to describe unique material mechanical tests, which can directly relate to the material parameters needed in the model²²⁻²⁶.

2.2 APPROACH

The mechanical test program was based largely on the GVIPS testing rational, using both an advanced directionally solidified alloy and its single crystal counterpart. The alloys tested were directionally solidified Rene 142 and single crystal Rene N6. Rene 142 is described in US patent 5,173,255²⁷ while the RN6 description is embodied in US patents 5,270,123²⁸ and 5,455,120²⁹.

All tests were performed from the same production qualified master heat for each alloy. Castings were provided by PCC's Development Facility in Minerva, Ohio. Both 0.5 inch diameter rods and 3/8 inch thick plate were cast. Single crystal primary orientations were held to within 15 degrees.

The specific test goals were as follows:

- Provide a basis for the development of the model parameters for the GVIPS and Single Crystal models and test the validity of these treatments.
- Demonstrate the utility of the Castelli, Arnold and Saleeb²⁴ test methodologies in Test Laboratories with advanced testing capabilities while extending these tests to the high temperature regime of OEI operation
- Design a test to simulate an OEI event.

Two GE approved Testing Laboratories were utilized in the program. These were Material Characterization Laboratory (MCL) in Scotia, NY, and Metcut Research Incorporated in Cincinnati, OH; both are routinely utilized by General Electric for critical mechanical tests.

2.3 TENSILE/RELAXATION TEST PROCEDURE

Three types of tensile/stress relaxation tests were performed at MCL including:

- 1A.) Tensile test strained to 2% strain followed by 2 hours relaxation. The 1A test matrix included testing at 1600°F, 1800°F, 2000°F, 2100°F, 2200°F, 2250°F and 2300°F at strain rates of 1.0E-06/s, 1.0E-05/s, 1.0E-03/s and 1.0E-01/s. Rene 142's upper test limit was 2250°F.
- 1B.) Tensile test strained to 1% strain followed by 2 hours relaxation, then strained to 2% followed by 2 hours relaxation. The 1B test matrix included testing at 1800°F, 2000°F, and 2200°F at strain rates of 1.0E-05/s, 1.0E-03/s and 1.0E-01/s. Rene 142's upper test limit was 2250°F.
- 1C.) Tensile test strained to 0.5% strain followed by 2 hours relaxation, then strained to 1% followed by 2 hours relaxation, then strained to 2% followed by 2 hours relaxation. The 1C test matrix included testing at 1600°F, 1800°F, 2000°F, 2100°F and 2200°F at strain rates of 1.0E-05/s, 1.0E-03/s and 1.0E-01/s.

An example of the three tensile relaxation test types is given in Figure 2-1 for R142 at 1800°F and 1.0E-05/s strain rate.

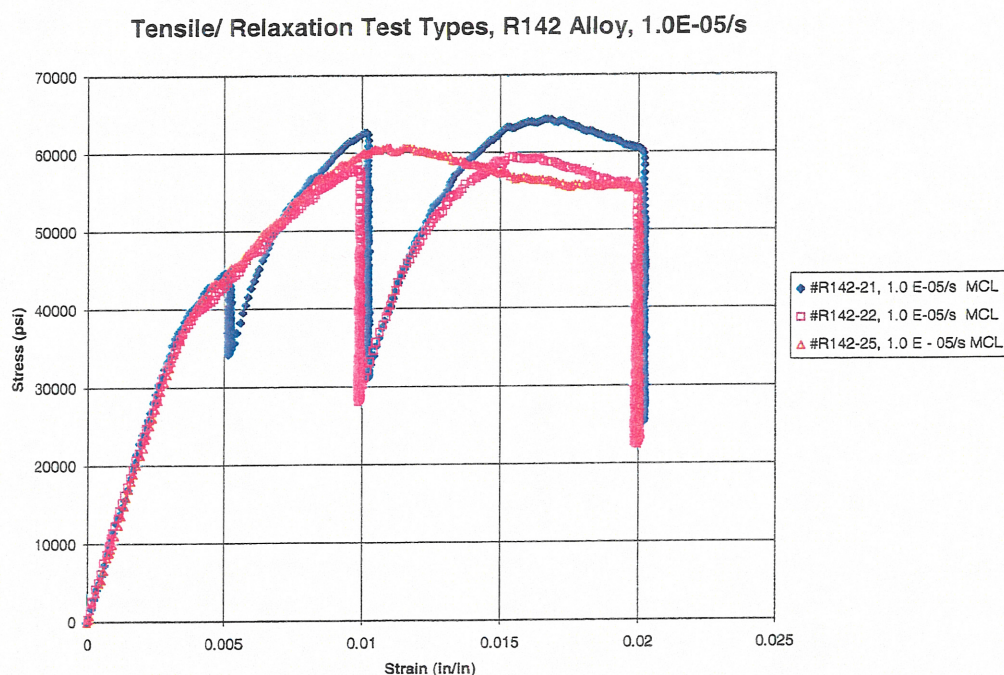


Figure 2-1. Rene 142 Tensile Relaxation Behavior At 1800°F And 1.0E-05/s Strain Rate.

MCL's test specimen geometry was a standard threaded 0.200 inch diameter specimen with a 0.750 inch smooth gage section. These were machined from the cast rod stock. The specimens were bare, since both R142 and RN6 have excellent oxidation resistance. MCL used standard MTS servo-hydraulic LCF type test stands at strain rates of 1.0E-03 and greater. Low-pressure surface contact type extensometry was used to measure strain and provide the control signal for constant strain rate control. The slow strain rate tests were performed on MCL custom designed electro-mechanical test machines. These use a stepper motor to turn a ball screw which drives an actuator up and down and can be programmed for stroke, load or strain control. The same extensometer set-up is used with these machines.

Metcut performed a similar test matrix except, generally without relaxation, and about 50% of the tests were run to failure. Metcut utilized a standard threaded 0.160 inch diameter specimen with a 0.750 inch gage section. These specimens were machined from the cast plate stock and were coated with a Pt-Al diffusion coating. Note that the primary dendrite spacings and microstructures for plate and rod were comparable. Metcut's tests were performed on a standard Instron screw type machine using Instron Series 9 software. The extensometer set-up was similar to MCL's and both vendors maintained a maximum temperature delta along the gage of 2°F through 2100°F and 3°F above this temperature.

2.4 TENSILE/RELAXATION TEST RESULTS

In general there was excellent agreement between both vendors as Figure 2-2 confirms. This is a plot of the 0.2% flow stress for Rene N6 over the entire temperature strain rate space.

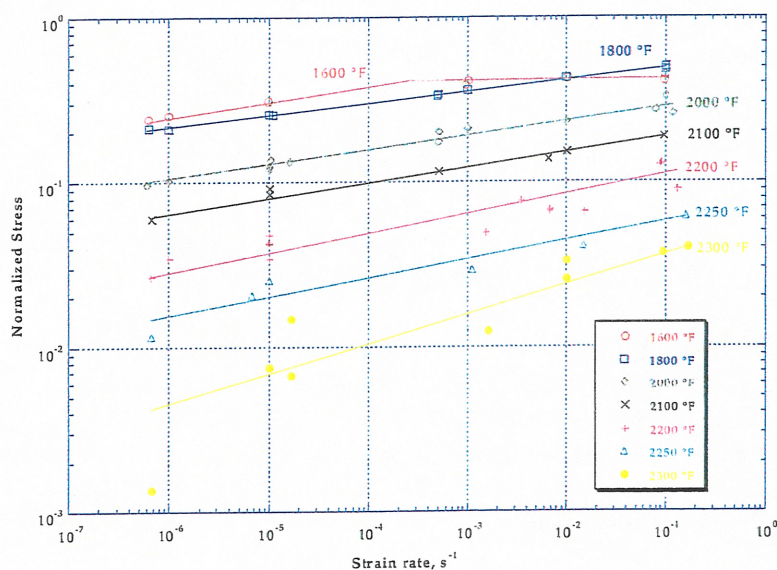


Figure 2-2. Rene N6 0.2% Yield Strength Behavior. Data From Both Test Vendors Is Plotted.

Each vendor encountered problems. At MCL, data recording and control issues were encountered, especially at the 1.0E-01/s strain rate. Here it was discovered that the control computer required a CPU with equivalent speed to at least a 166 MHZ Pentium chip. MCL logged data at a 100 points per second rate while Metcut utilized 50 points per second.

Both vendors ran into load train resonance at critical temperature - strain rate thresholds. Metcut, with the smaller test specimen, encountered vibration, set in motion by the machine's acceleration, at 1800°F and 1.0E-1/s. The Metcut fix was to switch to "position" control, which afforded a slower ramp up rate at the start of the test. In position control, an "end cutter" or location sensor on the crosshead controls crosshead speed. Strain rate is calculated using the effective gage length. The strain is still measured by the extensometer. Figure 2-3 shows a comparison between extensometer strain rate control and position strain rate control in the resonance regime.

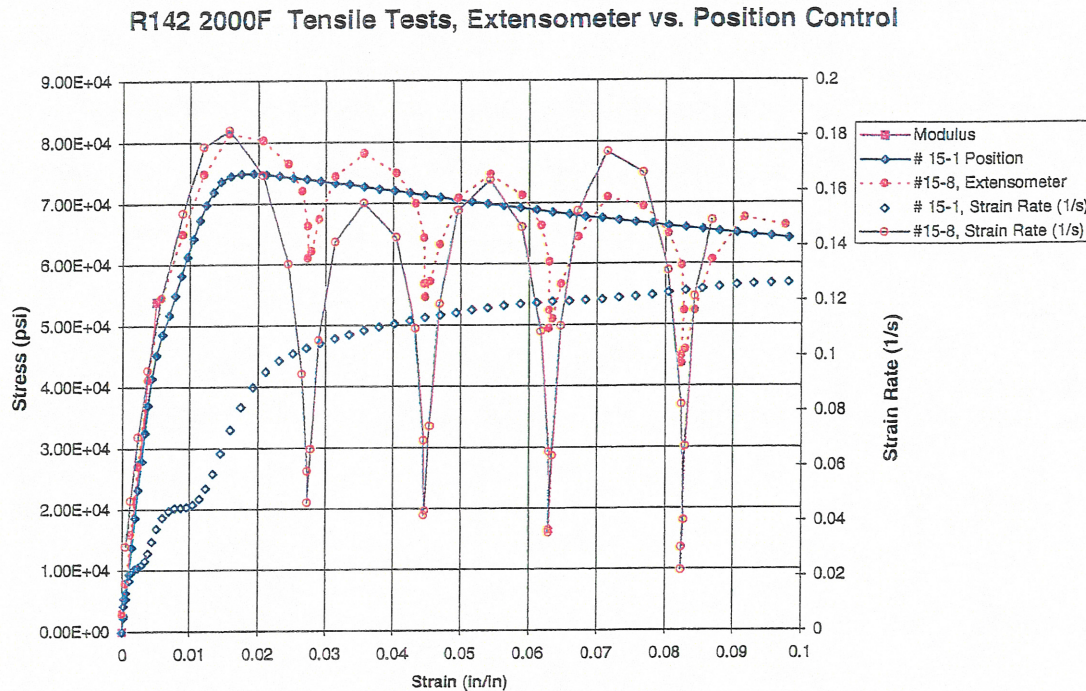


Figure 2-3. Two Tensile Tests From Metcut Comparing Extensometer Versus Position Strain Rate Control In Rene 142 At 2000°F And Nominal 1.0 E-01/S Strain Rate.

For MCL this problem was encountered at 2000°F and 1.0E-03/s. At MCL a switch to the electro-mechanical machine helped to reduce but not eliminate the problem. Unfortunately, the electro-mechanical apparatus has an upper strain rate limit of 1.0 E-03/s, so the problem persisted at the highest strain rate conditions. Here, data smoothing routines helped in the more moderate resonance cases. It is believed that an appropriate strain rate acceleration schedule or some system damping design would have been of benefit.

Another nuisance encountered at high temperatures was a cyclic "noise" signal picked up while measuring the low loads encountered at elevated temperatures. As such it was most pronounced during stress relaxation. Figure 2-4 shows a typical event, where the top curve is the data and the bottom curve is just the isolated noise. These events were intermittent and random in nature. No noise source was ever identified, and often a simple sine curve provided an excellent fit to the phenomenon.

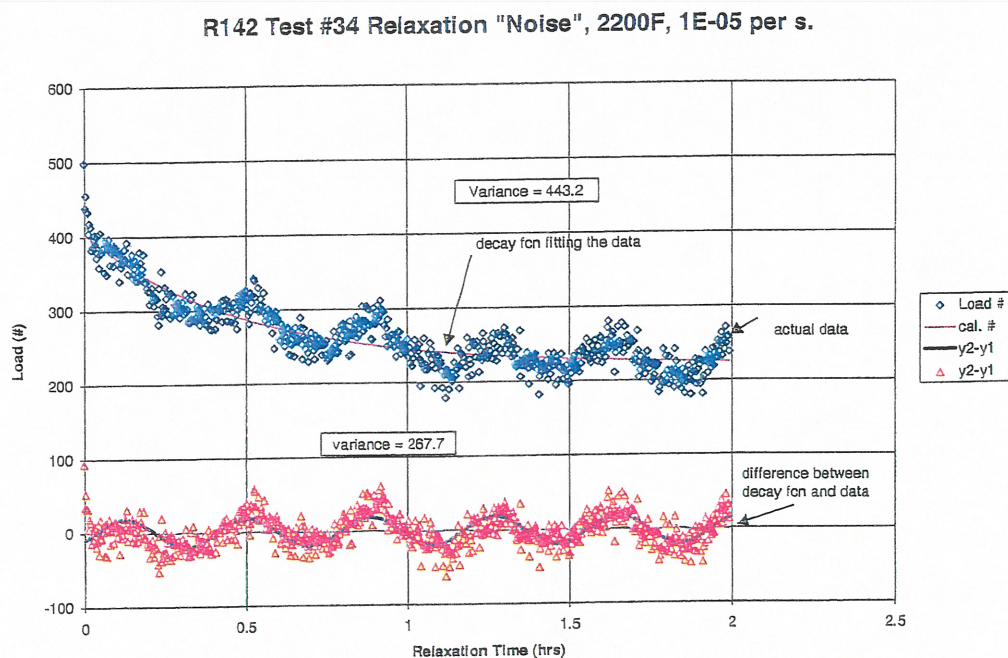


Figure 2-4. Cyclic Noise Occasionally Noted During Tensile Relaxation Test At Low Loads.

2.5 CREEP TESTS

MCL's electro-mechanical test machines offered constant stress creep capability with controlled strain rate loading schedules. Data was accumulated from the true test start, and all plastic deformation was recorded. This test apparatus was well suited for stress change testing. An example of constant stress creep response of R142 at 1800°F is given in Figure 2-5. Also included in this figure is a cyclic stress change test.

Metcut performed standard constant load creep tests per ASTM E139 using the Vertex data control and logging system. Loading curves are automatically calculated and plastic strain recorded. Strain measurements were performed with transducers with a tolerance less than 0.0001 inch. Since the true stress increases with extension in the constant load tests, these prove to have shorter lives as Figure 2-6 shows. Overall, the MCL test technique proved more reliable and provided less creep scatter.

The following test matrix represents the final valid data content suitable for model analysis. Defective tests (with incompletely recorded data, extensometer/transducer slippage and equipment failure) have been set aside.

Temperature	1600°F	1800°F	2000°F	2100°F	2200°F	2250°F	2300°F
	Number Of Test Points						
Constant Load R142	12	11	10	12	9	9	8
Constant Stress R142	8	9	7	3	8	3	3
Constant Load RN6	9	8	9	8	9	9	7
Constant Stress RN6	7	6	7	3	4	3	3

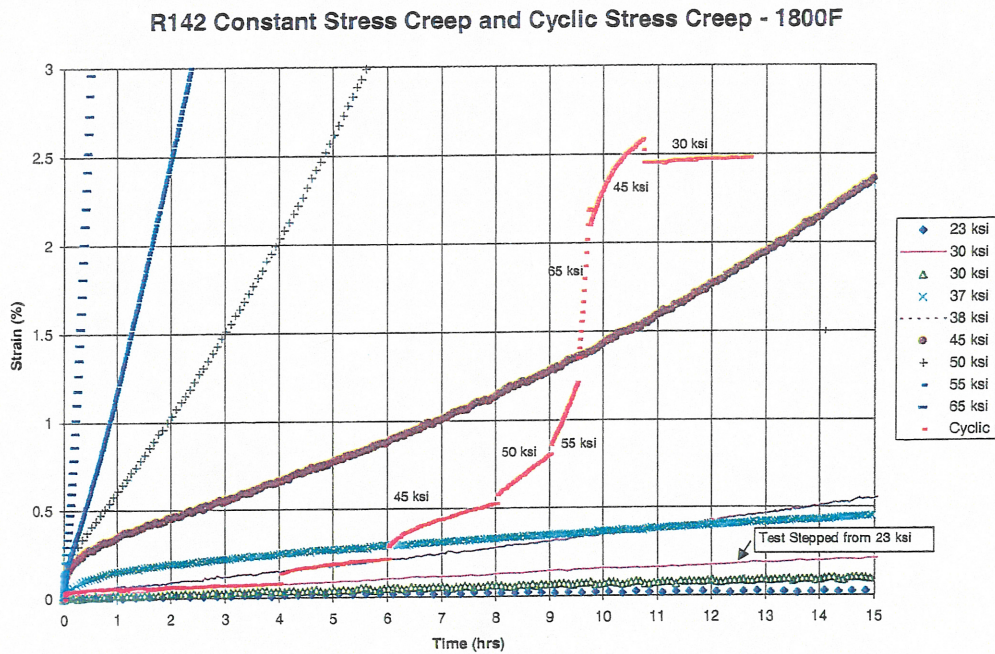


Figure 2-5. Rene 142 Constant Stress Creep Data At 1800°F.

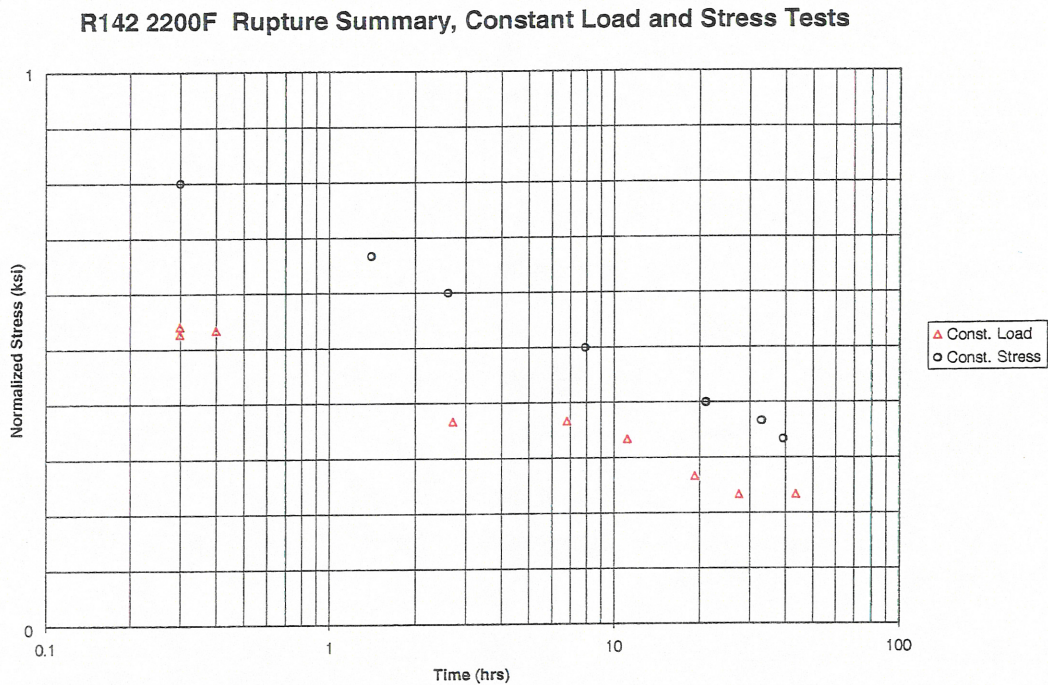


Figure 2-6. Rene 142 Creep Rupture Behavior At 2200°F.

2.6 MIXED CREEP-PLASTICITY TESTS

Since the state variable approach treats classical plasticity and creep as inelastic strain, a “mixed mode” test type can prove useful in validation of the procedure. This means that starting a test either first in a tensile mode then switching to creep or vice versa becomes a bench mark

test. One test of each type was completed at 1600°F, 1800°F, 2000°F and 2200°F. An example of this type of test is given in Figure 2-7.

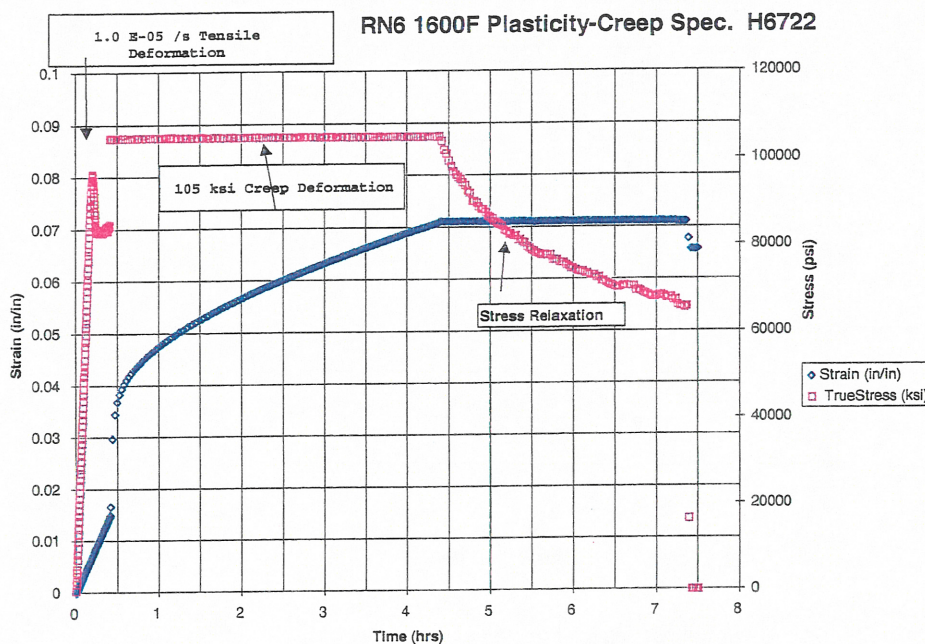


Figure 2-7. Rene N6 "Mixed Mode" Test Starting In Tensile Deformation, Switching To Creep, Then Ending In Stress Relaxation.

2.7 SIMULATED OEI EVENT

A special test was designed to simulate the brief OEI over temperature event. This test was set up on an MCL electro-mechanical test stand fitted with a custom designed igniter furnace. Care was taken to control temperature during the brief over temperature "spikes". Basically the test was started in the normal constant stress mode. Just prior to the over temperature, the mode is changed to load control. After the temperature spike is complete and once thermal stabilization has occurred, the mode is switched back to constant stress. Multiple spikes at different temperature levels can be programmed and executed. Figure 2-8 shows a complete test performed on R142 where four 200°F over temperature simulation "spikes" were performed and after the last spike, the temperature was raised 100°F. Figure 2-9 shows a double spike event on an expanded scale. In this figure, the thermal expansion recovery is apparent. A total of eleven tests were performed with 9 on Rene 142 and 2 on Rene N6.

2.8 RESULTS AND CONCLUSIONS

The test types described by Castelli, Arnold and Saleeb²⁴ can be performed at commercial test sources which have state-of-the-art test technology. Several key points were learned during this effort including;

- Control software expertise is paramount
- Resonance problems at high strain rate need to be addressed
- Noise and signal to noise limitations at high temperatures are always present
- Control computers must be fast and bug free.

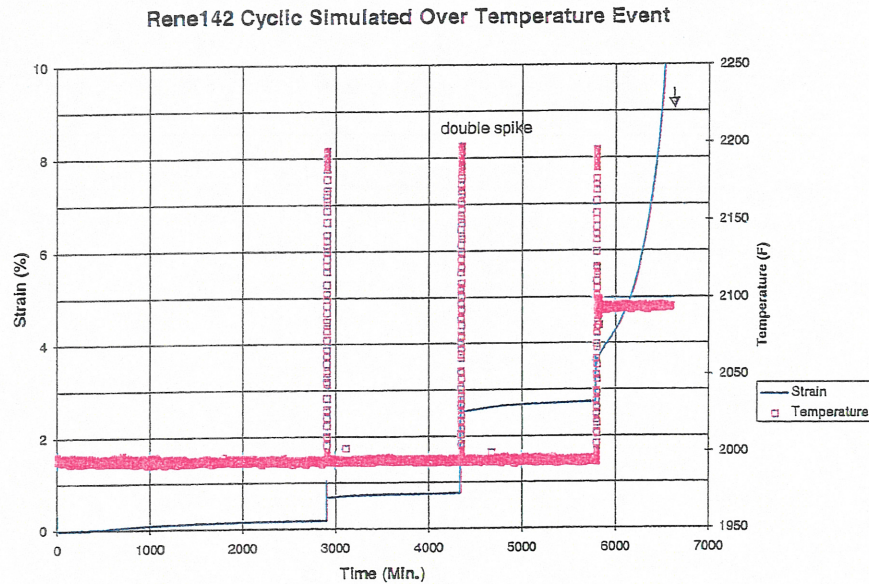


Figure 2-8. Rene 142 Simulated OEI Test

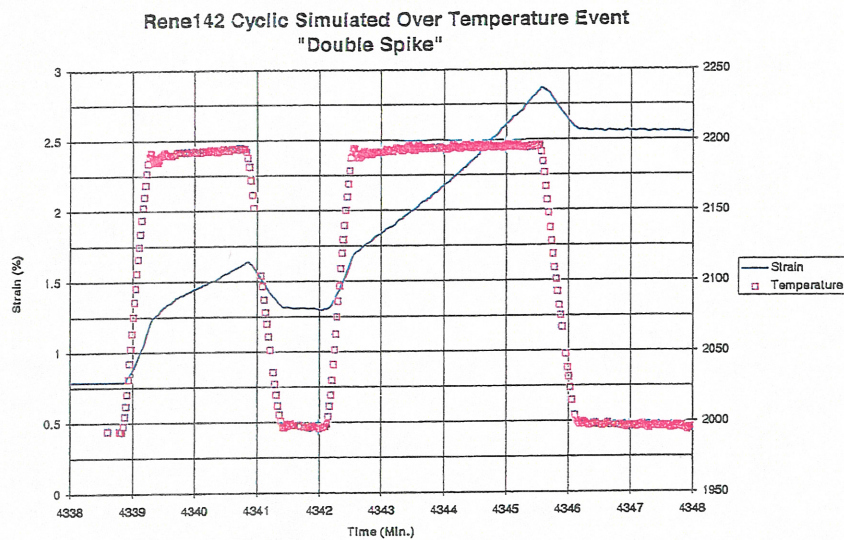


Figure 2-9. Consecutive 2 And 3 Minute Temperature Spikes. The Thermal Expansion Recovery Strain Is Also Apparent After Each Spike.

It is envisioned that future material characterization studies will focus on these new test types which extract more fundamental material information, while providing tests which more accurately duplicate service environments.

3.0 SINGLE CRYSTAL MODELS

3.1 INTRODUCTION

The need for accurate constitutive modeling stems from the desire to have accurate life prediction models. This goal clearly depends upon understanding the failure process under the complex loading and temperature regimes found in gas turbines. However the life models all depend on the state of stress and/or strain at critical component locations as input parameters. Thus a major part of the life analysis rests on the results of a finite element analysis of the component with an accurate material model to give accurate estimates of the stress and strain at critical sites in the component.

The objective of this research is to develop a useful, accurate constitutive model to predict the stress and inelastic strain response of the single crystal alloy Rene N6 under the load and temperature conditions found in high performance gas turbines, and implement this model in a finite element code that can be used for structural life prediction.

This section contains a review of the relevant material characteristics of Rene N6, the modeling approach (discussed in detail in Appendix B), and a few examples of results for Rene N6. The section ends with discussion of the additional work that is needed to satisfactorily complete the above objective.

3.2 REVIEW OF RELEVANT MATERIAL CHARACTERISTICS

The elastic and inelastic properties, and deformation mechanisms characteristic of cubic crystals including Rene N6 are much different than traditional polycrystalline alloys as described in Appendix A. Both elastic and inelastic response exhibits cubic symmetry. The mechanical response depends on the orientation of the applied loads and the properties in tension and compression are different when the temperature is below and above about one half of the absolute melting temperature. As temperature increases the anisotropy decreases and the material is close to isotropic as the temperature approaches the melting temperature.

The elastic properties change significantly with orientation and Poisson's ratio can even change sign. The inelastic properties also exhibit strong orientation dependence with inelastic effects like creep, stress relaxation and strain recovery, and the response depends on the rate of the applied loads. Even at the same temperature and strain rate the tensile response can vary widely with orientation. The shapes of the tensile curves are all different and the ultimate stress can vary by 100% or more.

The active deformation mechanisms by which inelastic deformation occurs fall into three general classifications: slip, diffusion, and rotation (see Appendices A3 and A4). Slip results from shear stresses propagating dislocations on the crystallographic planes, and active slip systems result in the tension-compression and orientation properties. Diffusion processes increase with increasing temperature resulting in climb of dislocations and the formation of new gamma-gamma prime structures or rafts. Rotation of the crystallographic planes can occur during slip to accommodate the deformation and boundary conditions simultaneously when the crystal is loaded in a single slip orientation. This type of effect can occur at the blade attachment site. Rotation changes the local shear stresses and active slip systems and can lead to very large deformations.

3.3 MODELING APPROACH

A unified constitutive equation similar to that discussed in more detail in Appendix C is used to model Rene N6. Since at least some slip is present at all temperatures the basis of the approach is to model the slip in each slip plane and each slip direction. Cubic crystals have four octahedral planes with two sets of three slip directions, and three cube planes with one set of slip directions on each plane resulting in thirty possible slip systems (see Appendix A4). The number of active slip systems depends on the temperature and orientation of the applied load. The slip system equations in Appendix A4 are written in the principal coordinates of the cubic crystal, so all external loads and boundary conditions must be transformed to the principal coordinates of the crystal lattice before using the slip equations.

There are three slip system constitutive models, one for each of the three sets of slip directions. The tension-compression asymmetry results from extended dislocations in the first octahedral slip system and the shear stresses resulting in the asymmetry are part of the slip system model. The first octahedral slip system model and cube slip system model together give the orientation effects. Creep at high temperature and low stress produce slip in the second octahedral slip system and this effect is modeled with third the constitutive equation.

Three sets of state variable evolution equations are used with three slip system models (see Appendix A5). There is a back stress variable to model balance between strain hardening dynamic recovery observed in tensile and cyclic loading. Temperature effects are included through a scalar drag stress that is developed to give the initial hardness (resistance to inelastic flow) and long thermal softening resulting from diffusion. The maximum value of the back stress (or extent of dislocation pileups) strongly depends on temperature and the local stress on the slip plane in the slip direction. The third state variable is used to characterize the maximum back stress in creep and high strain rate loading.

A systematic method has been developed to determine the constitutive parameters from tensile, creep and fatigue data (see Appendix A6). The slip equations (Appendix A4) are used to determine the local stresses and slip rates in each active slip system from the observed test data. These local values are used with the inelastic flow (slip) model and evolution equations in a specific order to evaluate and verify the parameters at each step in the process. The parameter evaluation method has been automated through the use of EXCEL spread sheets and FORTRAN codes.

3.4 RECOMMENDATIONS FOR FUTURE WORK

The results to date have been very encouraging, and models for the tensile and tertiary creep response are in place. However these results are for one orientation, $\langle 001 \rangle$, and one temperature, 2000°F. To achieve the objective, it is necessary to achieve the following results:

- 1.) Experimentally evaluate the response in other orientations to determine the anisotropy parameters in the model. It is necessary to have a complete working model to evaluate the response in the blade attachment site. Thus, it is necessary to have tensile, compressive and creep data in the $\langle 011 \rangle$ and $\langle 111 \rangle$ orientations and different strain rates to determine all the anisotropy parameters. Further it would be helpful to have some tensile and creep data in other orientations to verify the model.

- 2.) Extend the model to other isothermal temperatures above and below 2000°F. This is the first step in developing a model for simultaneous mechanical and thermal cycling. Above 2000°F the response will be more dependent on temperature than stress. The slip orientation effects will become less important but orientation dependent raft microstructures will develop from preferred paths of diffusion. Below 2000°F slip becomes more important and the slip models may have some different features above and below 2000°F.
- 3.) Extend the model to include thermal history effects and over temperature excursion effects. The first step is to use the results for modeling the response at each of the isothermal temperatures described in 2) above. This will include evaluating the thermomechanical response by interpolation. However our experience has shown that this approach will not be totally adequate since the interaction between low temperature slip and high temperature climb can produce extra hardening that is not seen in isothermal testing. These studies will require the some special thermomechanical experiments to isolate the extra hardening effects.
- 4.) Finite element implementation of the model, which is the last step necessary to establish a whole blade structural model. An earlier version of the model has been implemented in a twenty node brick. The new constitutive model will be implemented in the twenty node brick and used with finite element model of the temperature history distribution to establish the structural response of a blade and it attachment. The modeling approach will be experimentally verified with a simple structure.

4.0 GVIPS MODEL FOR DS MATERIAL

4.1 MODEL BASICS

A detailed evaluation of the GVIPS model and the COMPARE code is given in Appendix B. As described in the appendix, the model has been under development for several years and has been applied successfully by Arnold, et. al.. In addition to the basic model, a code called COMPARE has been developed which performs nonlinear optimization to determine the constants required by the model. As shown in the appendix the model is quite nonlinear, and it is convenient to have an automated tool with the capability to perform this non-linear optimization. As opposed to the development for the single crystal model given in Section 3.0, GVIPS is based on a potential function theory, and consequently, the anisotropic predictions are determined by parametric representations in the transverse and longitudinal directions. Since the anisotropic behavior predicted by a single crystal model is different than the behavior that would be observed for a DS material, the GVIPS model was thought to be appropriate for the DS Rene' 142 data that was tested during this program. Unfortunately, since the testing was entirely in the longitudinal direction, the anisotropic predictions of the model were not evaluated during this phase of the contract.

4.2 MODEL CONSIDERATIONS

As discussed in Sections 2.0 and 3.0, the turbine blade materials being considered in this program exhibit a substantial amount of tertiary creep. Prior to this program, GVIPS, like most constitutive models did not have a method to predict tertiary creep. During the course of this program, Dr. Arnold of NASA Lewis Research developed the capability to predict tertiary creep in the GVIPS model.

4.3 MODEL PREDICTIONS

Figures 4-1 through 4-8 show a correlation obtained from COMPARE of some Rene' 142 data tested at 1600°F. Note that these are the results from four tensile and four creep tests that were used in getting the correlation. COMPARE has a limitation that only eight experiments can be evaluated at a time. As shown, with the exception of the data for the high strain rate (Figure 4-8) the correlation is pretty good. The data was analyzed using the version of the theory that does not have tertiary creep. Consequently, the data and the predictions deviate at longer times (an attempt was made to cull out the tertiary creep data before the COMPARE analyses were made; as shown in the figures, some tertiary creep was still included in the analyses).

Creep Response

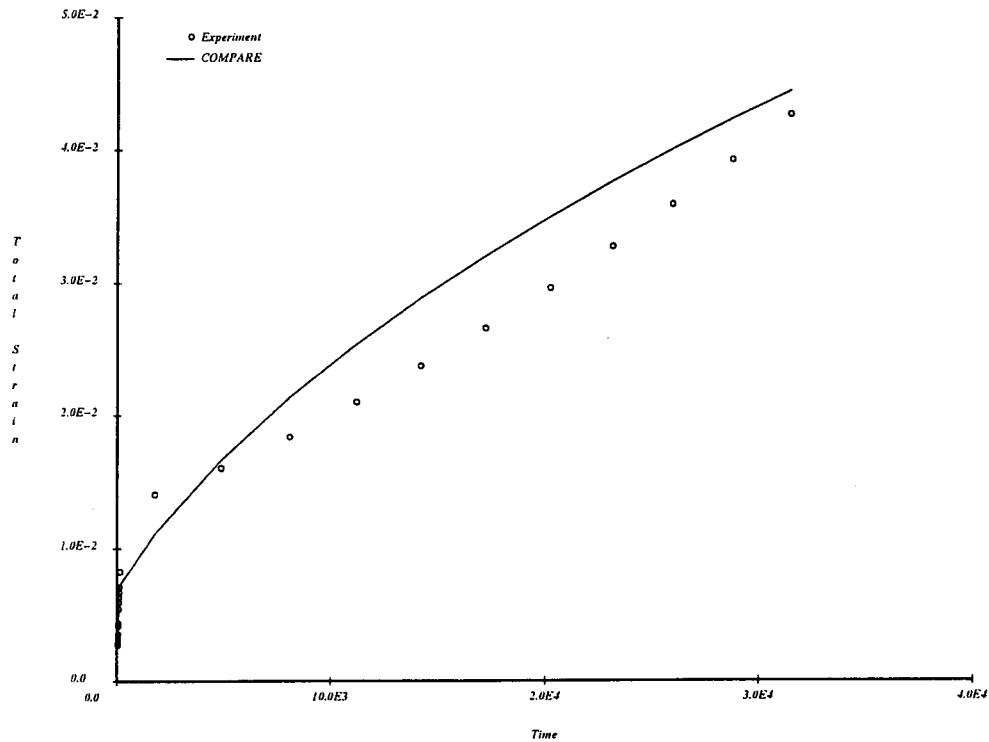


Figure 4-1. Comparison Of Predicted Versus Data For Creep Test 57, Rene' 142 At 1600°F - 91 KSI.

Creep Response

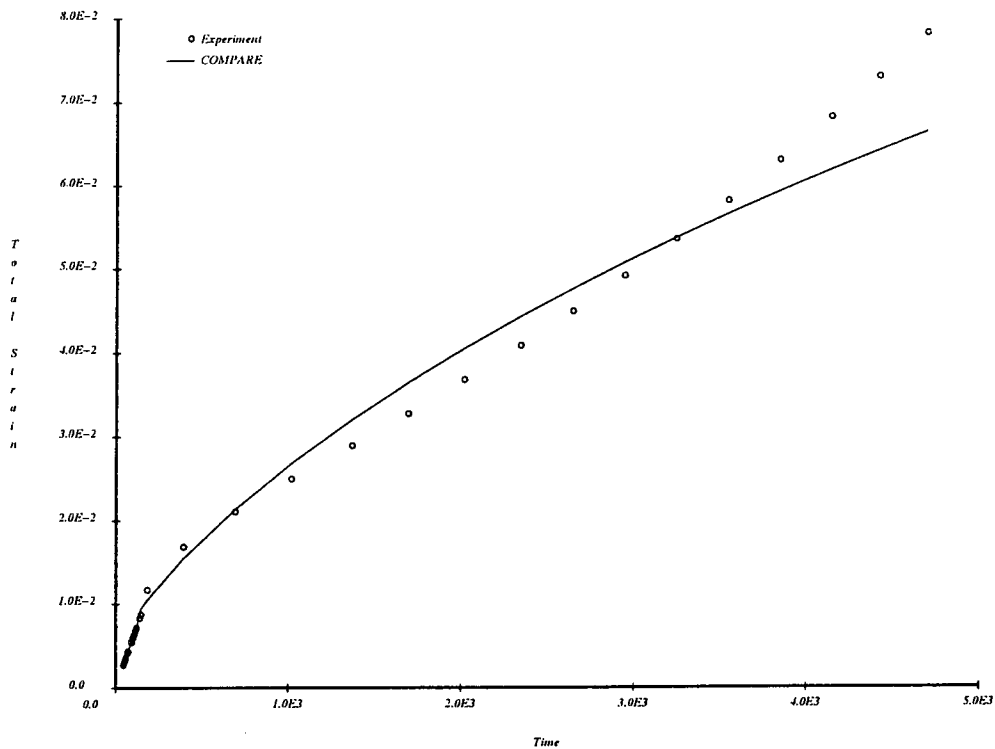


Figure 4-2. Comparison Of Predicted Versus Data For Creep Test 60, Rene' 142 At 1600°F - 111 KSI.

Creep Response

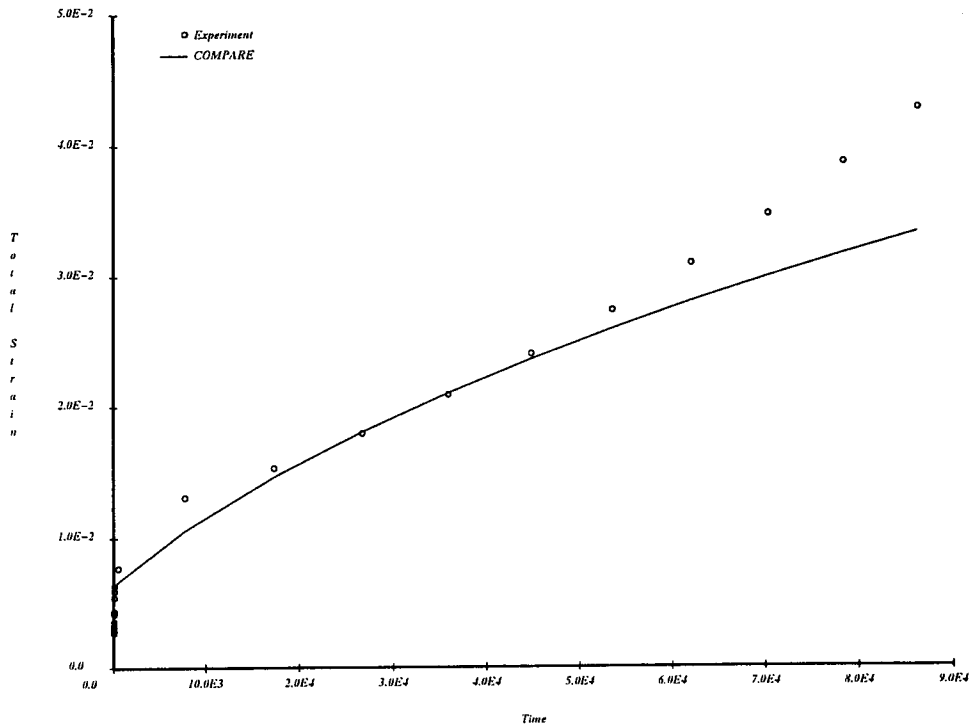


Figure 4-3. Comparison Of Predicted Versus Data For Creep Test 65, Rene' 142 At 1600°F – 80 KSI.

Creep Response

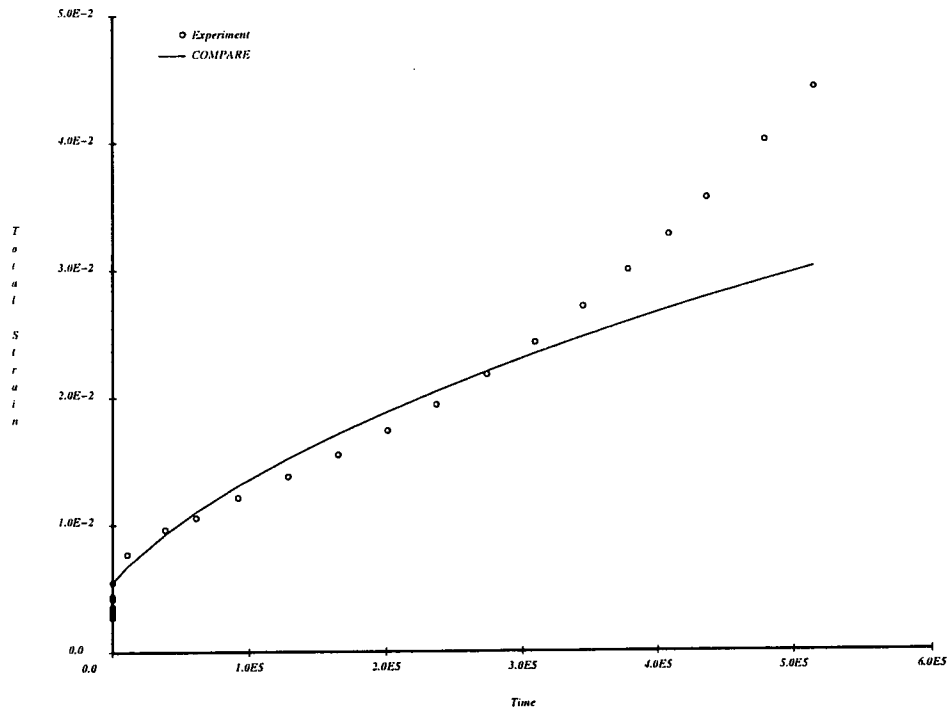


Figure 4-4. Comparison Of Predicted Versus Data For Creep Test 66, Rene' 142 At 1600°F – 69 KSI.

Tensile Response

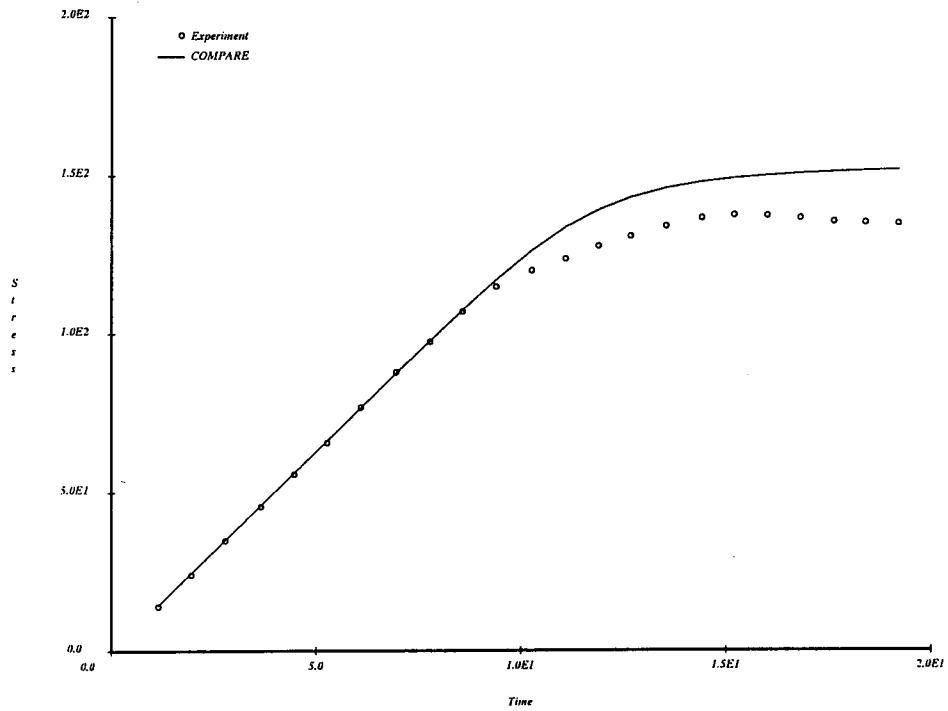


Figure 4-5. Comparison Of Predicted Versus Data For Tensile Test 11, Rene' 142 At 1600°F - 1n/1n/Sec.

Tensile Response

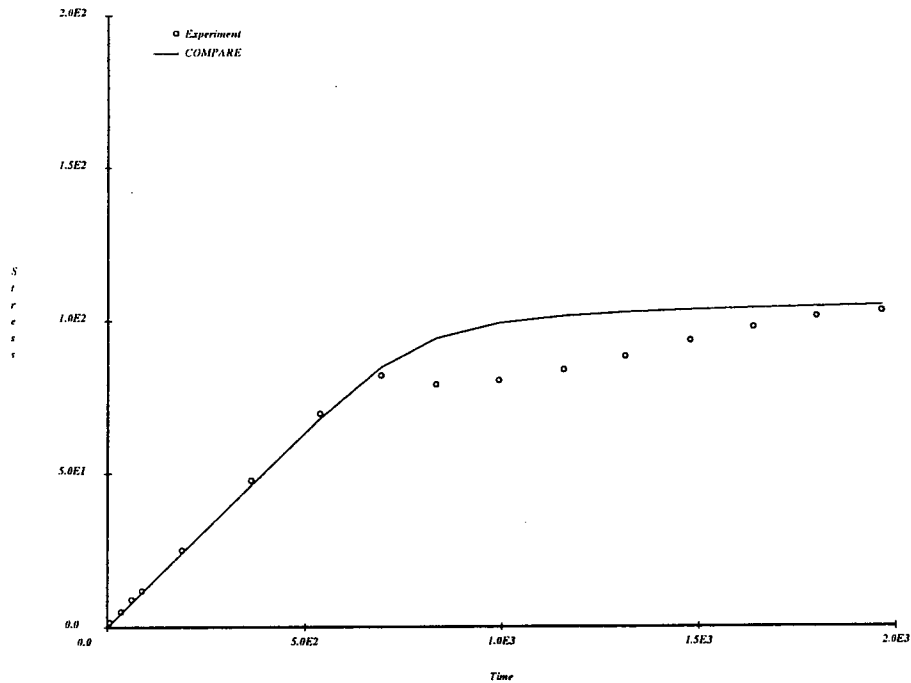


Figure 4-6. Comparison Of Predicted Versus Data For Creep Test 26, Rene' 142 At 1600°F - 1E-5 1n/1n/Sec.

Tensile Response

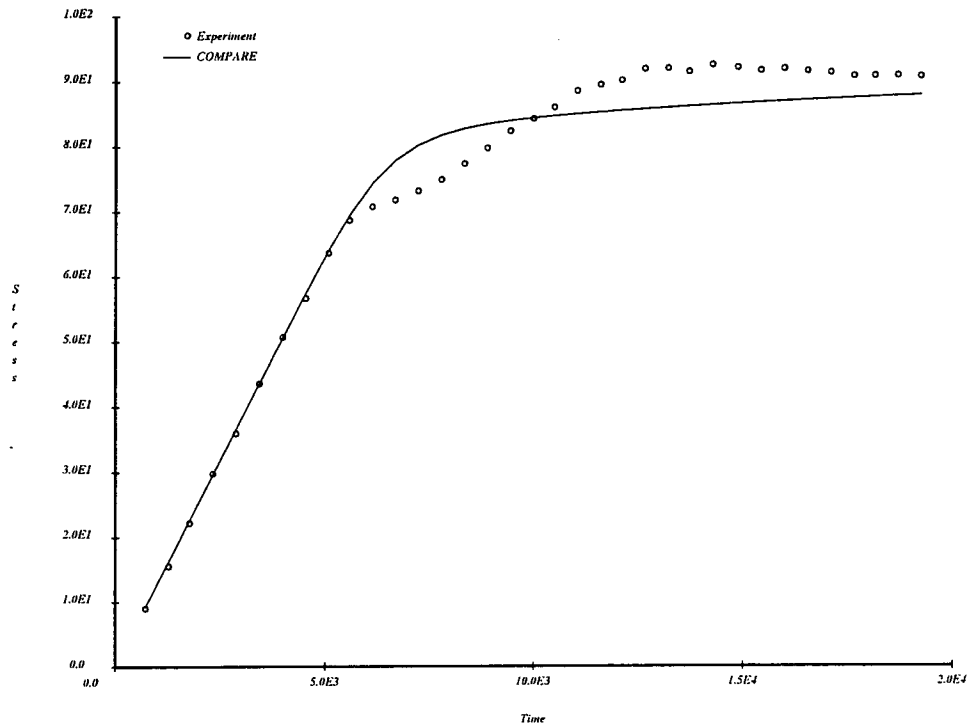


Figure 4-7. Comparison Of Predicted Versus Data For Tensile Test 5, Rene' 142 At 1600°F – 1E-6 In/In/Sec.

Tensile Response

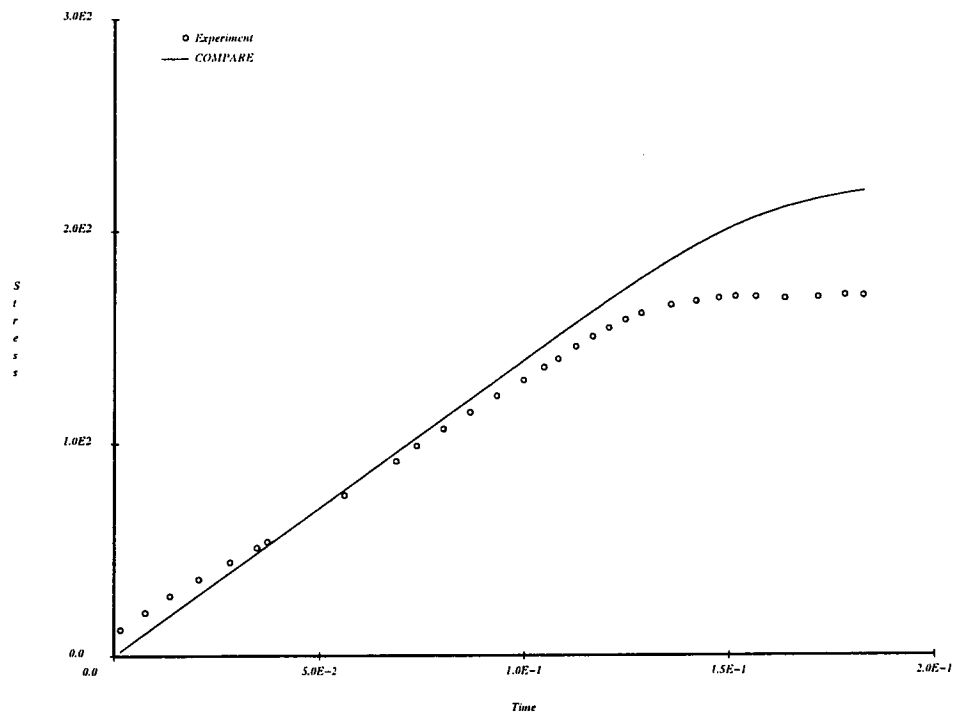


Figure 4-8. Comparison Of Predicted Versus Data For Tensile Test 67, Rene' 142 At 1600°F – 1E-1 In/In/Sec.

5.0 REFERENCES

1. Stouffer, D.L. and Dame, T.L. (1996). Inelastic deformation of metals: Models, mechanical properties, and metallurgy, John Wiley and Sons Inc., New York.
2. McLean, M. (1983). Directionally solidified materials for high temperature service, *The Metals Society*, London.
3. Bodner, S.R. and Partom, Y. (1972). A large deformation elastic plastic analysis of a thick walled spherical shell, *Journal of Applied Mechanics*, Vol. 39. Pp. 751-757.
4. Bodner, S.R. and Partom, Y. (1975). Constitutive equations for elastic-viscoplastic Strain hardening materials, *Journal of Applied Mechanics* Vol. 24. p.283.
5. Miller, A. K. (1976). An inelastic constitutive equation for monotonic, cyclic and creep deformation: Part 1: Equations development and analytical procedures, Part 2: application to 304 stainless steel, *Journal of Engineering Materials and Technology*, Vol. 98H, pp. 97-113.
6. Chaboche, J.L. (1986). Time dependent constitutive theories for cyclic plasticity, *International Journal of Plasticity*, Vol. 2, No. 2, pp. 149-188.
7. Krieg, R.D., Swearingen, J.C., and Rohde, R. (1978). A physically based internal variable model for rate dependent plasticity, in *Inelastic Behavior of Pressure Vessel and Piping Components*, ASME/CSME, PVP-PB-028, p. 15.
8. Miller, A.K. (1978). An inelastic constitutive model for monotonic, cyclic, and creep deformation: Part I: Equations, development, and analytical procedures: Part II: Application to type 304 stainless steel, *Journal of Engineering Materials and Technology*, Vol. 98, No. 2, pp. 97-113.
9. Robinson, D.N. (1978). A unified creep plasticity model for structural metals at high temperature, *ORNL TM-5969*.
10. Lee, D. and Zaverl, F. (1978). A generalized strain rate dependent constitutive equation for anisotropic metals, *Acta Metallurgica*, Vol. 26, pp. 1771-1780.
11. Walker, K.P. (1981). Research and development program for nonlinear structural modeling with advanced time-temperature dependent constitutive relationships, *NASA CR 165533*.
12. Robinson, D.N. and Swindeman, R.W. (1982). Unified creep plasticity constitutive equations for 2 ¼ Cr-1 Mo steel at elevated temperature, *ORNL TM-8444*.
13. Ramaswamy, V.G. (1986). A constitutive model for the inelastic multiaxial cyclic response of a nickel base superalloy Rene' 80, *NASA CR 3998*.
14. Ramaswamy, V.G., Stouffer, D.C., and Laflen, J.H. (1990). A unified constitutive model for the inelastic uniaxial response of Rene' 80 at temperatures between 538°C and 982°C, *Journal of Engineering Materials and Technology*, Vol. 112.
15. Swanson, G. (1984). Life prediction and constitutive model for hot section anisotropic materials program, *Contract NAS3-23939, Monthly Report PWA-5968-9*, August.
16. Swanson, G. (1984). Life prediction and constitutive model for hot section anisotropic materials program, *Contract NAS3-23939, Monthly Report PWA-5968-10*, September.

17. Dame, L.T. and Stouffer, D.C. (1985). Anisotropic constitutive model for nickel base single crystal alloys: model development and finite element implementations, *NASA CR-175015*.
18. Dame, L.T., and Stouffer (1988). A crystallographic model for nickel base single crystal alloys, *Journal of Applied Mechanics*, Vol. 55, pp. 325-331.
19. Sheh, M.Y., and Stouffer, D.C. (1988). Anisotropic constitutive modeling of nickel base single crystal superalloy, *NASA CR 182157*.
20. Milligan, W.W. (1986). Yielding and deformation behavior of the single crystal nickel base superalloy PWA 1480, *NASA CR 175100*.
21. Sheh, M.Y. and Stouffer, D.C. (1990). A crystallographic model for tensile and fatigue response of Rene' N4 at 982°C, *Journal of Applied Mechanics*, Vol. 57. Pp. 25-31.
22. Arnold, S.M., Saleeb, A.F., and Wilt, T.E. (1993). A modeling investigation of thermal and strain induced recovery and nonlinear hardening in potential based viscoplasticity, *NASA TM-10622*.
23. Arnold, S.M., Saleeb, A.F., and Castelli, M.G. (1995). A fully associative, nonisothermal, nonlinear kinematic, unified viscoplastic model for titanium alloys, *NASA TM-106926*.
24. Castelli, M.G., Arnold, S.M., and Saleeb, A.F. (1994). Specialized deformation tests for the characterization of a viscoplastic model: Application to a titanium alloy. *ASTM Symposium on Fiber, Matrix and Interface Properties, Phoenix*.
25. Saleeb, A.F., and Arnold, S.M. (1997). A general reversible hereditary constitutive Mode 1: Part 1: Theoretical developments, *NASA TM-107493*.
26. Arnold, S.M., Saleeb, A.F., and Castelli, M.G. (1997). A general reversible hereditary constitutive Mode 1: Part II: Application to a titanium alloy, *NASA TM-107494*.
27. Ross, E.W and O'Hara, K. S. US Patent 5,173,255, 12/22/92
28. Walston, W.S., Ross, E.W, O'Hara, K. S. and Pollack, T. M., US Patent 5,270,123, 12/14/93
29. Hopgood A. A. and Martin J. W (1986), The Creep Behavior of a Nickel Based Crystal Superalloy, *Mat Sci Engr*, 82:27-36.
30. Lall C., Chin S., and Pope D. (1979), The Orientation and Temperature Dependence of the Yield Stress of Ni₃(Al, Nb) Single Crystals, *Metallurgical Transactions*, 10A:1323
31. Kear, H. B., G. R. Leverant and J. M. Objak (1969). An analysis of creep induced intrinsic/extrinsic fault pairs in a precipitation hardened nickel-base alloy, *Transactions American Society of Metals*, Vol. 62, pp. 639-650.
32. Leverant, G. R. and H. B. Kear (1970). The mechanism of creep in a γ' precipitation hardened nickel-base superalloy at intermediate temperatures, *Metallurgical Transactions*, Vol. 1, pp. 491-498.
33. Leverant, G. R., H. B. Kear and J. M. Objak (1973). Creep of precipitation hardened nickel-base superalloy single crystals at high temperature, *Metallurgical Transactions*, Vol. 4, pp. 355-362.

34. MacKay, R. A. and R. D. Maier (1982), "The influence of Orientation on the Stress Rupture Properties of Nickel Base Superalloy Single Crystals", Metallurgical Transactions 13A, pp1747-1754
35. Milligan W. W., and Antolovich S. D. (1989) "Deformation Modeling and Constitutive Modeling of Anisotropic Superalloys", NASA CR 4215
36. Miner, R., Voigt, R., Gayda, J. and Gabb, T. (1986) "Orientation and Temperature Dependence of Some Mechanical Properties of the Nickel Base Single Crystal Alloy Rene N4: Part 1, Tensile Behavior", Metallurgical Transactions, 17A, p 491.
37. Miner, R., Voigt, R., Gayda, J. and Gabb, T. (1986) "Orientation and Temperature Dependence of Some Mechanical Properties of the Nickel Base Single Crystal Alloy Rene N4: Part 3, Tension/Compression Anisotropy", Metallurgical Transactions, 17A, p 507.
38. Paidar, V., Pope, D. P., and Vitek, V. (1984) "A Theory of the Anomalous Yield Behavior in LI2 Ordered Crystals", Acta Metall V23.3, pp 435-448
39. Pollock T. and Argon A.(1991) "Creep Resistance of Superalloy Single Crystals: Experiments and Modeling", Modeling the Deformation of Crystalline Solids, Ed. T. C. Lowe, A. D. Rollet, P. S. Follansbee and G. S. Daehn, The Minerals, Metals and Materials Society
40. Sheh, M. Y., and Stouffer, D. C., (1990), "A Crystallographic Model for Tensile and Fatigue Response of Rene' N4 at 982C", ASME Journal of Applied Mechanics., 57, pp 25-31
41. Verhoeven, J. D. (1975) Fundamentals of Physical Metallurgy, J. Wiley & Sons, New York
42. Arnold, S. M. and Saleeb, A. F. (199⁴) "On the Thermodynamic Framework of Generalized Coupled Thermoelastic-Viscoplastic Damage Modeling", Int. Journal of Plasticity V 10.3, pp263-278.
43. Saleeb, A. F. and Wilt, T. E. (1993) "Analysis of the Anisotropic Viscoplastic Damage Response of Composite Laminates" Int. J. Numerical Methods Eng., V. 36, pp.1629-1660.
44. Saleeb, A. F., Gendy, A. S., Wilt, T. E. and D. A. Throwbridge, "COMPARE, Constitutive Material Parameter Estimator Users Guide", Version 1.0, University of Akron, Department of Civil Engineering.

APPENDIX A – SINGLE CRYSTAL MATERIALS

A.1 INTRODUCTION

Nickel base single crystal alloys are used in rocket and gas turbine engines because their high temperature properties are superior to those of polycrystalline nickel base superalloys. In high temperature applications, grain boundaries in polycrystalline alloys provide passages for diffusion and oxidation. Eliminating grain boundaries, and the grain boundary strengthening elements, produces materials with superior high temperature fatigue and creep properties compared to conventional superalloys. However the absence of grains make the alloys anisotropic or orientation dependent.

This appendix contains a discussion of the elastic and inelastic anisotropic properties of single crystal alloys and the details of the development of the constitutive equations that are used to predict their response. The appendix begins with an overview of the elastic properties and models and the tensor structure of the equations. Sections A.3 and A.4 contain a review of the material properties and the three general classes of deformation mechanisms (slip, diffusion, and rotation) that control the mechanical properties. The kinematic equations to determine the stresses on the slip planes and the accumulated inelastic strain from the slip in each of the active slip planes are given in Section A.5. Section A.6 describes the constitutive equations used to model slip and diffusion at the slip plane level, and the method used to determine the material parameters is given in Section A.7.

A.2 MATERIALS WITH ELASTIC CUBIC SYMMETRY

Single metallic crystals with face centered cubic or body centered cubic lattice structure exhibit anisotropic elastic response (Dame and Stouffer 1985, 1988). Materials with cubic symmetry can be shown to have only three independent elastic constants. The three independent elastic constants are designated the elastic modulus, shear modulus and Poisson's ratio. The elastic compliance matrix is

$$\begin{Bmatrix} \varepsilon_{xx} \\ \varepsilon_{yy} \\ \varepsilon_{zz} \\ \gamma_{xy} \\ \gamma_{xz} \\ \gamma_{yz} \end{Bmatrix} = \begin{bmatrix} \frac{1}{E} & \frac{-\nu}{E} & \frac{-\nu}{E} & 0 & 0 & 0 \\ \frac{-\nu}{E} & \frac{1}{E} & \frac{-\nu}{E} & 0 & 0 & 0 \\ \frac{-\nu}{E} & \frac{-\nu}{E} & \frac{1}{E} & 0 & 0 & 0 \\ 0 & 0 & 0 & \frac{1}{G} & 0 & 0 \\ 0 & 0 & 0 & 0 & \frac{1}{G} & 0 \\ 0 & 0 & 0 & 0 & 0 & \frac{1}{G} \end{bmatrix} \begin{Bmatrix} \sigma_{xx} \\ \sigma_{yy} \\ \sigma_{zz} \\ \tau_{xy} \\ \tau_{xz} \\ \tau_{yz} \end{Bmatrix} \quad (A2.1)$$

This matrix appears identical to the matrix of elastic constants for isotropic materials. However, the elastic constants E , ν , and G are all independent, and the components of the matrix are a function of orientation. Equation A2.1 is only valid when the loading is in the principal directions of the material or parallel to the edges of the fcc or bcc cubic lattice. Therefore it is necessary to establish a method to transform Equation A2.1 to other orientations. The results will be used

to determine the elastic constants from three tensile tests on test samples with arbitrary orientation relative to the principal axes of the material, and to determine the compliance matrix in other orientations.

Let us establish the elastic stress strain response of a test specimen with the arbitrary orientation e_1'' relative to the crystal axes. The vector e_1'' is oriented in space by two successive rotations. First is a positive rotation θ about the e_3 axis so that the e_1 basis in the principal direction of the material is transformed into the e_1' basis. Second is a negative rotation ϕ about e_2' transforming e_1' into e_1'' . The two transformation matrices are

$$\begin{bmatrix} e_1' \\ e_2' \\ e_3' \end{bmatrix} = \begin{bmatrix} \cos \theta & \sin \theta & 0 \\ -\sin \theta & \cos \theta & 0 \\ 0 & 0 & 1 \end{bmatrix} \begin{bmatrix} e_1 \\ e_2 \\ e_3 \end{bmatrix} \quad (\text{A2.2a})$$

and

$$\begin{bmatrix} e_1'' \\ e_2'' \\ e_3'' \end{bmatrix} = \begin{bmatrix} \cos \phi & 0 & \sin \phi \\ 0 & 1 & 0 \\ -\sin \phi & 0 & \cos \phi \end{bmatrix} \begin{bmatrix} e_1' \\ e_2' \\ e_3' \end{bmatrix}. \quad (\text{BA2.2b})$$

The constitutive Equation (A2.1) relative to the principal axes of the crystal can be written in matrix notation as

$$[\gamma'] = [S'] [\sigma'] \quad \text{where} \quad [S'] = [R][Q][R]^{-1} [S][Q]^{-1} \quad (\text{A2.3})$$

The transformation matrix $[Q]$ can be established by expanding the transformation rule defined by Equation (A2.3) in a six dimensional vector with the components arranged as

$$[S'] = \begin{Bmatrix} \sigma_{11}' \\ \sigma_{22}' \\ \sigma_{33}' \\ \sigma_{12}' \\ \sigma_{13}' \\ \sigma_{23}' \end{Bmatrix}$$

Evaluating the transformation matrix for a rotation about the x_3 axis as described in Equation (A2.2a) gives

$$[Q] = \begin{bmatrix} c^2\theta & s^2\theta & 0 & 2cs\theta & 0 & 0 \\ s^2\theta & c^2\theta & 0 & -2cs\theta & 0 & 0 \\ 0 & 0 & 1 & 0 & 0 & 0 \\ -cs\theta & cs\theta & 0 & c^2\theta - s^2\theta & 0 & 0 \\ 0 & 0 & 0 & 0 & c\theta & -s\theta \\ 0 & 0 & 0 & 0 & s\theta & c\theta \end{bmatrix}$$

where notation c and s are used for cosine and sine, respectively. The inverse transformation is obtained by letting $[Q^{-1}] = [Q(-\theta)]$, and it can also be shown that $[R][Q][R]^{-1} = [Q]^{-T}$ so the transformed compliance matrix can be expressed as

$$[S'] = [Q]^{-T} [S] [Q]^{-1} \quad (A2.4)$$

The compliance matrix can be determined in the e'_i basis by substituting $[Q]^{-1}$ into Equation (A2.4). The non-zero components in the compliance matrix are

$$\begin{aligned} S'_{11} &= \frac{1}{E'} = \frac{1}{E} \left(\cos^4 \theta + \sin^4 \theta \right) + \left(\frac{1}{G} - \frac{2\nu}{E} \right) \cos^2 \theta \sin^2 \theta \\ S'_{12} &= \frac{-\nu'}{E'} = \left(\frac{2}{E} - \frac{1}{G} \right) \cos^2 \theta \sin^2 \theta - \frac{\nu}{E} \left(\cos^4 \theta + \sin^4 \theta \right) \\ S'_{14} &= \frac{\eta'}{E'} = \left(\frac{1}{G} - 2 \frac{1+\nu}{E} \right) \cos \theta \sin \theta \left(\cos^2 \theta - \sin^2 \theta \right) \\ S'_{44} &= \frac{1}{G'} = 8 \left(\frac{1+\nu}{E} \right) \cos^2 \theta \sin^2 \theta + \frac{1}{G} \left(\cos^2 \theta - \sin^2 \theta \right)^2 \end{aligned} \quad (A2.5)$$

Equation (A2.5) shows when the material is loaded with a tensile stress in the $e'_3 = e_3$ direction, $\bar{\sigma}' = [0 \ 0 \ \sigma_0 \ 0 \ 0 \ 0]^T$, the transverse strains are independent of orientation and the test specimen remains round. If a tensile specimen is loaded in the e'_1 direction,

$\bar{\sigma}' = [\sigma_0 \ 0 \ 0 \ 0 \ 0 \ 0]^T$, then the diametrical response does depend upon orientation. The elastic modulus, E' , and shear modulus, G' , vary with orientation and Poisson's ratio and ν' , even changes sign. There is coupling between the shear and normal stress and strain components defined by the Lekhnitski coefficients of mutual influence. In any arbitrary orientation, e'_j the matrix of elastic constants can become fully populated and include shear stress-shear strain coupling. The shear stress-shear strain coupling constants are called the Chentsov coefficients. Thus with only three independent elastic constants, the elastic response of a cubic symmetric material is significantly more complex than the elastic response of an isotropic material.

The axial compliance in the e''_1 direction can be determined so that $\varepsilon''_1 = S''_{11} \sigma_0$ for a tensile stress vector $\bar{\sigma}'' = [\sigma_0 \ 0 \ 0 \ 0 \ 0 \ 0]^T$. Following the same steps for the second rotation, Equation (A2.2b), the compliance of a tensile specimen in the e''_1 direction can be found from

$$\begin{aligned} S''_{11} &= \frac{1}{E''} = \\ &= \frac{1}{E} \left[\cos^4 \phi \left(\cos^4 \theta + \sin^4 \theta \right) + \sin^4 \phi \right] + \left(\frac{1}{G} - \frac{2\nu}{E} \right) \left[\cos^4 \phi \cos^2 \theta \sin^2 \theta + \cos^2 \phi \sin^2 \theta \right] \end{aligned} \quad (A2.6)$$

Since there are only two independent material parameters in S'_{11} and S''_{11} , from Equations (A2.5) and (A2.6) respectively,

$$\frac{1}{E} \quad \text{and} \quad \left(\frac{1}{G} - \frac{2\nu}{E} \right),$$

tensile compliance measurements from the principal orientation and two other different orientations can not be used to determine the three elastic parameters E , G and ν . Recalling that a round specimen remains round when loaded in one of the three principal directions, a tensile test in a principle direction can also be used to measure E and ν . A second tensile test in an arbitrary orientation then gives the shear modulus G . The accuracy of the parameters depends on the reliability of the orientation measurements.

These results were established for evaluating the elastic constants for materials with cubic symmetry. Transforming the stiffness or compliance matrices in structural calculations is awkward. It is frequently easier to transform stress or strain from the global coordinates to the principal coordinates of the material, use the constitutive equation in the principal coordinates of the material, and then transform the result back to the global coordinates. Care should be exercised when using both engineering and tensor strain.

A.3 INELASTIC SLIP MECHANISMS

The orientation and tension-compression asymmetry properties can be explained from the active slip systems and dislocation mechanisms. There may be up to three families of active slip systems depending on the orientation of the applied load and temperature. Milligan and Antolovich (1989) reported for PWA 1480 for strain rates other than creep (typically greater than 10^{-4} sec^{-1}) that:

- Below about 600°C deformation occurs due to slip on the octahedral planes, $[111]$ planes, in the 12 directions similar to the $[101]$ direction. Octahedral slip is shown in Figure A-1 and corresponds to Slip Numbers 1 to 12 in Tables A-1 and A-2.
- Between about 600°C and 850°C deformation occurs simultaneously by octahedral slip and cube slip. Cube slip occurs on the three planes similar to $[001]$ in the two directions similar to the $[011]$ direction (6 slip systems) as defined in Figure A-2 and Slip Numbers 25 to 30 in Tables A-1 and A-2.
- Above about 850°C the strong effect of climb and cross slip reduces the dependence on orientation and the particular slip systems that are active.

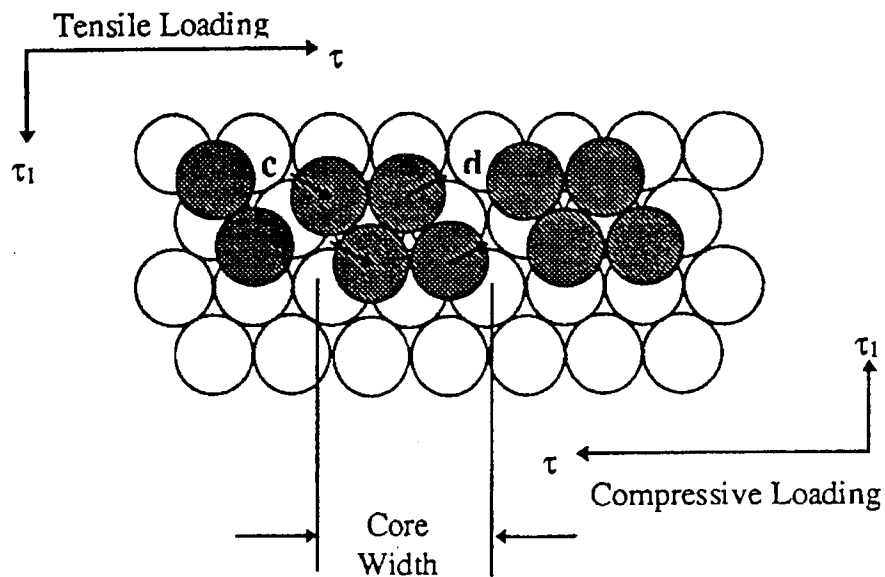


Figure A-1. Effect Of Tensile And Compressive Stresses On The Core Width Of An Extended Dislocation.

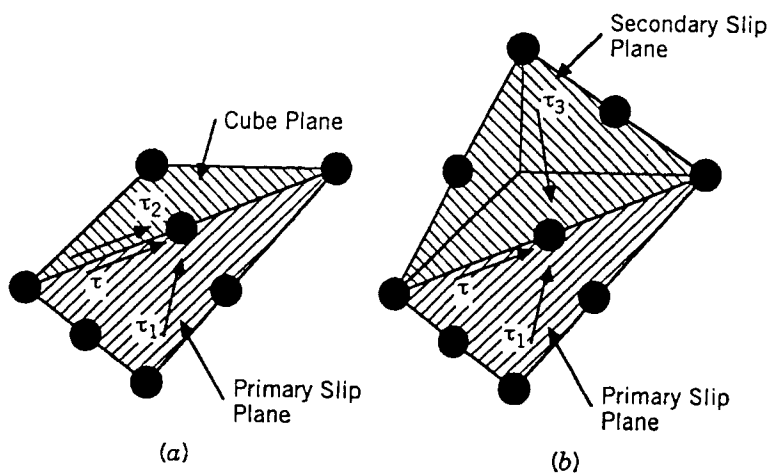


Figure A-2. Definitions Of The Stresses, τ .

Table A-1. Distribution Of The Resolved Shear Stress In Each Slip System Of An FCC Crystal For A Loading Of 100 MPa In The [100], [110], [111], And [321] Directions.

Slip No.	[100]	[110]	[111]	[321]
1	408.25	408.25	.00	349.93
2	.00	-408.25	.00	-174.96
3	408.25	.00	.00	174.96
4	-408.25	.00	.00	-116.64
5	-408.25	.00	-272.17	-291.61
6	.00	.00	-272.17	-174.96
7	408.25	.00	-272.17	.00
8	.00	.00	.00	.00
9	408.25	.00	-272.17	.00
10	.00	-408.25	-272.17	-349.93
11	-408.25	-408.25	-272.17	-466.57
12	-408.25	.00	.00	-116.64
13	-235.70	235.70	.00	.00
14	471.40	235.70	.00	303.05
15	-235.70	-471.40	.00	-303.05
16	-235.70	.00	-314.27	-269.37
17	-235.70	.00	157.13	33.67
18	471.40	.00	157.13	235.70
19	-235.70	.00	157.13	.00
20	471.40	.00	-314.27	.00
21	-235.70	.00	157.13	.00
22	471.40	235.70	157.13	336.72
23	-235.70	235.70	157.13	134.69
24	-235.70	-471.40	-314.27	-471.40
25	.00	353.55	471.40	454.57
26	.00	353.55	.00	151.52
27	.00	353.55	471.40	404.06
28	.00	353.55	.00	202.03
29	.00	.00	471.40	252.54
30	.00	.00	.00	-50.51

Table A-2. Correspondence Between The Slip Number In Table A-1 And Slip Directions On The Crystal Planes.

Slip No.	Slip Plane	Slip Direction
Octahedral Slip $a/2\langle 110 \rangle\{111\}$		
1	[1 1 1]	[1 0 -1]
2	[1 1 1]	[0 -1 1]
3	[1 1 1]	[1 -1 0]
4	[-1 1 -1]	[1 0 -1]
5	[-1 1 -1]	[1 1 0]
6	[-1 1 -1]	[0 1 1]
7	[1 -1 -1]	[1 1 0]
8	[1 -1 -1]	[0 -1 1]
9	[1 -1 -1]	[1 0 1]
10	[-1 -1 1]	[0 1 1]
11	[-1 -1 1]	[1 0 1]
12	[-1 -1 1]	[1 -1 0]
Octahedral Slip $a/2\langle 112 \rangle\{111\}$		
13	[1 1 1]	[-1 2 -1]
14	[1 1 1]	[2 -1 -1]
15	[1 1 1]	[-1 -1 2]
16	[-1 1 -1]	[1 2 1]
17	[-1 1 -1]	[1 -1 -2]
18	[-1 1 -1]	[-2 -1 1]
19	[1 -1 -1]	[-1 1 -2]
20	[1 -1 -1]	[2 1 1]
21	[1 -1 -1]	[-1 -2 1]
22	[-1 -1 1]	[-2 1 -1]
23	[-1 -1 1]	[1 -2 -1]
24	[-1 -1 1]	[1 1 2]
Cube Slip $a/2\langle 110 \rangle\{100\}$		
25	[1 0 0]	[0 1 1]
26	[1 0 0]	[0 1 -1]
27	[0 1 0]	[1 0 1]
28	[0 1 0]	[1 0 -1]
29	[0 0 1]	[1 1 0]
30	[0 0 1]	[-1 1 0]

These results are consistent with the observations of Miner (1986, 1986b) for Rene N4 at 760, 870, and 982°C. Miner found only cube slip for loading near the [111] orientation, and only octahedral slip for loading near the [100] and [110] orientations.

The number of active slip systems similar to [111][101] depends on the orientation and magnitude of the applied load. The shear stress, τ , parallel to any slip system can be calculated from the applied tensile stress, σ , using Schmid's Law

$$\tau = \sigma \cos(\alpha) \cos(\beta) \quad (\text{A3.1})$$

where β is the angle between the tensile axis and the slip plane normal vector and α is the angle between the tensile axis and the slip direction. It can be shown, for the slip systems similar to $[111][101]$, that loading in the $[001]$ direction will activate eight slip systems simultaneously if the stress is equivalent to the critical resolved shear stress (CRSS). Loading in the $[110]$ direction will activate four simultaneous slip systems, whereas only one slip system will be activated for loading in the $[123]$ direction.

Next, slip on the octahedral plane occurs by the disassociation of a total dislocation into two partial dislocations. The atoms in the core of the extended dislocation have a different stacking sequence. The stacking fault energy controls the core width, and the small core widths have a greater potential for cross slip to a cube plane. In an ideal setting slip occurs by adding atoms to the core and removing atoms from the core. In practice, extended dislocation movements are disrupted by other dislocations, antiphase boundaries, cross slip, and climb at high temperatures.

In single crystals, Lall, Chin and Pope (1979) showed that extended dislocations create the tension-compression asymmetry because they behave differently in tension and compression. Consider a tensile load that creates a shear stress on an octahedral plane that is not parallel to the slip direction. This shear stress can be resolved into two components with one component parallel to the slip direction, τ , and one component normal to the slip direction, τ_1 , as shown in Figure A-1. During tensile loading in the $[001]$ direction, for example, the normal component of the shear stress, τ_1 , will increase the potential that atoms are added to the core, increase the resistance to cross slip, and increase the yield stress. When the applied stress is reversed, the shear stress $-\tau_1$ will favor adding atoms to the core and reduce the potential that atoms are removed from the core. Thus the core width is extended during tensile loading and reduced during compressive loading. Next recall that at temperatures below the critical temperature there are no stress in the cube slip systems. Thus dislocations that cross slip from the octahedral planes to the cube planes during tensile loading in the $[001]$ direction are pinned and their movement is restricted. At high temperatures the dislocations are not pinned on the cube planes and cross slip increases the potential for slip in the cube slip systems. Thus, the core width controls the potential for cross slip, and the response in tension and compression will be different.

The movement of extended dislocations can be influenced by other stresses in the crystal lattice. Lall, Chin and Pope (1979) also proposed that the stress on the cube plane, τ_2 , parallel to τ on the octahedral plane will promote cross slip from the octahedral plane to the cube plane, see Figure A-2. The potential for the cross slip is increased with increasing temperatures. The stress τ_2 is particularly important when the loading is near the $[111]$ orientation where the stresses on the cube plane may be larger than the octahedral stress. Paidar, Pope and Vitek (1984) later proposed that the stress normal to the slip direction on the intersecting octahedral plane (τ_3) also influences the core width. The effect of τ_3 is similar to that of τ_1 on the core width, and increasing values of τ_3 increase the potential for cross slip of the dislocation.

Milligan and Antolovich (1989) investigated the tensile and cyclic behavior of PWA 1480 in the temperature range from 20°C to 1093°C at strain rates of 0.50 and 50.0% per minute. They found two types of dislocation networks at high and low temperatures. At temperatures between approximately 20 and 760°C and for loading in the $[001]$ orientation with plastic strains up to 0.3 %, the dislocation network was dominated by pairs of extended dislocations shearing

the γ' phase. In this temperature range dislocations traveled through the γ' as closely spaced pairs. In contrast to the shearing mechanism at low temperature, a γ' bypass mechanism was observed at temperatures of 982°C and higher. For specimens tested to failure at 982°C there were high dislocation densities in the γ phase, and that deformation was controlled by looping or bypass of the γ' particles. Shearing of the γ' phase was also observed after a large increase in the matrix dislocation density and significant strain hardening. In the intermediate temperature range from 760°C to 927°C a transition from shearing to bypass was observed.

To summarize, deformation of single crystal occurs by slip in the octahedral and cube slip systems. The tension-compression asymmetry results from the propagation of partial dislocations that depend on four shear stress components, τ and τ_2 in the slip direction, and τ_1 and τ_3 that are normal to the slip direction. To use this information in constitutive modeling it is necessary to develop the equations for local stresses from the applied stress in a global or reference coordinate system. It will also be necessary to determine a representation for the inelastic strain resulting in the global coordinate system from the local slip in each slip system.

A-4 LATTICE ROTATION AND CREEP

The deformation discussed so far has been limited to small plastic deformations typical of low cycle fatigue applications. However, if the deformations are larger than 3 or 4%, such as found in creep and tensile loading, rotation of the crystallographic structure may occur during slip. The rotation occurs in single slip orientations to simultaneously accommodate the deformation and restraints at the boundary. For example, consider a tensile test of the single crystal tensile specimen oriented in a single slip orientation. The grips hold the ends of the specimen in a fixed alignment. During application of the load, slip will initiate on a number of parallel slip planes located close to the maximum shear stress, and slip bands will be observed on the surface of the specimen. As deformation progresses, continued slip would not be possible without rotation of the slip planes to accommodate the change in length of the specimen. Bending will occur near the grips to maintain continuity and alignment of the specimen. During elongation the slip planes rotate toward the tensile axis, and the angle between the slip plane and tensile axis decreases. As rotation continues a second slip plane will become oriented in a position to permit slip. When the stress on this plane reaches the critical resolved shear stress, slip will occur in a second slip system. Eventually the slip on the primary and secondary planes will become equal and duplex slip will occur (identical slip in both systems).

The rotation of a specimen in a single slip orientation can be plotted in a stereographic projection. Specimen D in Figure A-3a has one active slip system in the $[\bar{1}01]$ direction for loading in the $[123]$ as direction shown in Table A-1. The tensile force produces a rotation that moves the $[\bar{1}01]$ slip system vector toward the tensile axis at Point D, and the angle λ decreases in Figure A-3a. However, instead of rotating the stereographic projection toward Point D, it is more convenient to leave the stereographic projection fixed and rotate Point D toward the $[\bar{1}01]$ slip system. Using this approach, when Point D reaches Point 2, two slip systems ($[111][\bar{1}01]$ and $[111][011]$) will have the same stress and duplex slip will result. From Point 2 the specimen will rotate along the $[001]-[\bar{1}11]$ boundary to $[\bar{1}12]$, the point midway between $[\bar{1}01]$ and $[011]$ in the $[1\bar{1}1]$ plane (the vector sum of the two slip systems). The specimen will remain at this orientation until failure. Figure A-4a shows the directions of rotation along the $[001]-[\bar{1}11]$ boundary for a specimen starting in any orientation within the

stereographic triangle. Crystals with an initial orientation on the perimeter of the stereographic triangle will exhibit duplex slip upon loading, and rotate initially to the poles shown in Figure A-4a.

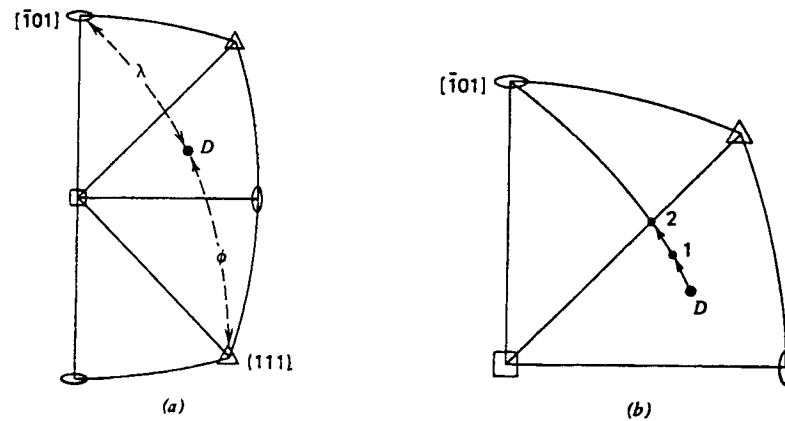


Figure A-3. Stereographic Projection Showing The Rotation Of A Tensile Specimen Loaded In A Single Slip Orientation.

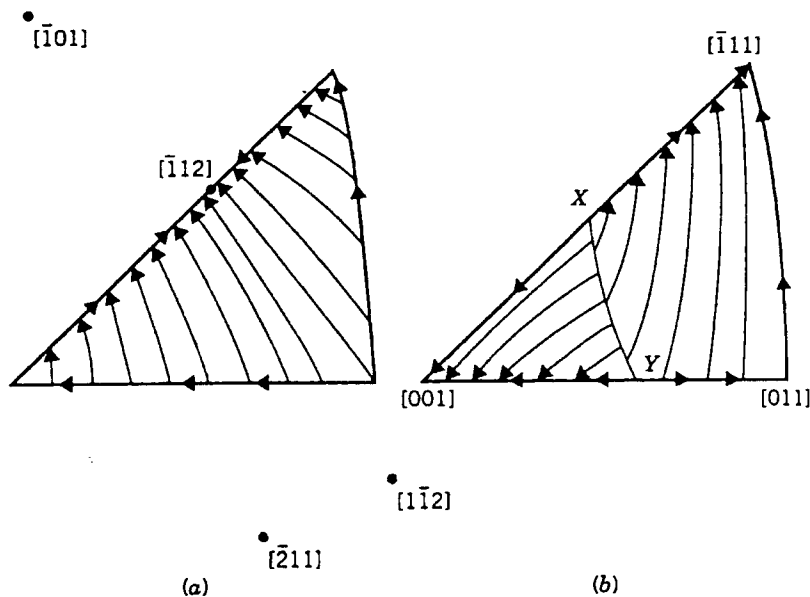


Figure A-4. Directions Of Rotation For Crystals Loaded In Single Slip Orientations In The Standard [001] Stereographic Triangle For The (A) [111][$\bar{1}11$] And (B) [111][112] Slip Systems.

Creep deformation at the higher stress levels, but below the yield stress, can occur by dislocation creep and dislocation glide. At lower values of stress, creep bulk diffusion occurs (Nabarro-Herring Creep). Single crystal creep is more complicated because the active slip system for dislocation creep or dislocation glide can change during creep or be different for different alloys. Leverant and Kear (1969, 1970, 1973) and MacKay and Maier (1982) reported

for Mar M200 and Mar M247, respectively, that primary creep and secondary creep occur in different slip systems. In particular, for temperatures near 750°C:

- Primary creep occurs by deformation in the slip systems similar to [111][112]. This is the second octahedral slip shown in Table A-2 and corresponds to Slip Numbers 13 to 24 in Table A-2.
- Secondary creep occurs by deformation in the slip systems similar [111][101].

However, Hopgood and Martin (1986) reported for SRR99 at 750 and 800°C that:

- Both primary and secondary creep occurred by deformation in the slip systems similar to [111][112].
- Deformation in the cube system has not been reported for creep near the [111] orientation.

Thus, it appears that primary creep occurs in the slip systems similar to [111][112], but the active slip system for secondary creep may be an alloy specific property. Lattice rotations for the [111][112] slip system are shown in Figure A-4b. The boundary X-Y is defined by the Schmid Factor $\cos(\lambda)\cos(\phi) = 0.427$ in Equation A3-1. For the [111][112] slip system, duplex slip only occurs along the [001]-Y and X- $[\bar{1}11]$ boundaries of the stereographic triangle.

Nickel base single crystals also exhibit a delay in the onset of creep for small values of stress. Pollock and Argon (1991) conducted a study of the creep resistance of CMSX-3 in the [001] orientation at temperatures between 800°C and 900°C and loads between 450 MPa and 600 MPa. There was no instantaneous straining on loading (elastic strains are subtracted out), and delays of 1.6×10^4 and 600 seconds were recorded for the tests at 800°C and 850°C, respectively. No delay was observed at 900°C, and lower stresses were found to produce longer incubation periods in the onset of primary creep. To document the process during the incubation period, a creep test was terminated during the delay period at 4.5×10^3 seconds. A typical micrograph shows that dislocations spread out to dislocation free regions from initial grown-in dislocation tangles. Primary creep is assumed to be initiated when an active deformation system is achieved by the meeting of dislocation loops.

A.5. KINEMATIC EQUATIONS FOR CRYSTALLOGRAPHIC SLIP

It is necessary to develop the equations for local shear stresses and local slip in each slip system for use in constitutive modeling (Dame and Stouffer, 1985, 1988). The stress vector t acting on some plane with an outward normal vector n is given by

$$\begin{bmatrix} t_1 \\ t_2 \\ t_3 \end{bmatrix} = \begin{bmatrix} \sigma_{11} & \sigma_{12} & \sigma_{13} \\ \sigma_{21} & \sigma_{22} & \sigma_{23} \\ \sigma_{31} & \sigma_{32} & \sigma_{33} \end{bmatrix} \begin{bmatrix} n_1 \\ n_2 \\ n_3 \end{bmatrix} \quad (A5.1)$$

where σ_{ij} are the stress components in a principal coordinate of the material (parallel to the right hand coordinate system in the [100], [010] and [001] orientations) at the point in question. The component of the stress, τ , in some direction p is then calculated from

$$\tau = [t_1 \ t_2 \ t_3] \cdot [p_1 \ p_2 \ p_3] \quad (\text{A5.2})$$

where p and n are unit vectors. The local shear stresses can be determined from Equations A5.1 and A5.2 for each of the 30 slip numbers given in Table A-1 and shown graphically in Figures A-1 and A-2. The result for the primary octahedral slip systems similar to $[111][\bar{1}01]$ is

$$\begin{bmatrix} \tau_1^{11} \\ \tau_1^{12} \\ \tau_1^{13} \\ \tau_1^{21} \\ \tau_1^{22} \\ \tau_1^{23} \\ \tau_1^{31} \\ \tau_1^{32} \\ \tau_1^{33} \\ \tau_1^{41} \\ \tau_1^{42} \\ \tau_1^{43} \\ \tau_1^{14} \\ \tau_1^{15} \\ \tau_1^{16} \\ \tau_1^{17} \\ \tau_1^{18} \\ \tau_1^{19} \\ \tau_1^{20} \\ \tau_1^{21} \\ \tau_1^{22} \\ \tau_1^{23} \\ \tau_1^{24} \\ \tau_1^{25} \\ \tau_1^{26} \\ \tau_1^{27} \\ \tau_1^{28} \\ \tau_1^{29} \\ \tau_1^{30} \end{bmatrix} = \begin{bmatrix} \tau^1 \\ \tau^2 \\ \tau^3 \\ \tau^4 \\ \tau^5 \\ \tau^6 \\ \tau^7 \\ \tau^8 \\ \tau^9 \\ \tau^{10} \\ \tau^{11} \\ \tau^{12} \end{bmatrix} = \frac{1}{\sqrt{6}} \begin{bmatrix} 1 & 0 & -1 & 1 & 0 & 1 \\ 0 & -1 & 1 & -1 & 1 & 0 \\ 1 & -1 & 0 & 0 & 1 & -1 \\ -1 & 0 & 1 & 1 & 0 & -1 \\ -1 & 1 & 0 & 0 & -1 & -1 \\ 0 & 1 & -1 & -1 & -1 & 0 \\ 1 & -1 & 0 & 0 & -1 & -1 \\ 0 & 1 & -1 & -1 & 1 & 0 \\ 1 & 0 & -1 & -1 & 0 & -1 \\ 0 & -1 & 1 & -1 & -1 & 0 \\ -1 & 0 & 1 & -1 & 0 & -1 \\ -1 & 1 & 0 & 0 & 1 & -1 \end{bmatrix} \begin{bmatrix} \sigma_{11} \\ \sigma_{22} \\ \sigma_{33} \\ \sigma_{12} \\ \sigma_{31} \\ \sigma_{23} \end{bmatrix} \quad (\text{A5.3})$$

The shear stresses in the slip systems similar to the secondary octahedral $[111][112]$ are given by

$$\begin{bmatrix} \tau_2^{11} \\ \tau_2^{12} \\ \tau_2^{13} \\ \tau_2^{21} \\ \tau_2^{22} \\ \tau_2^{23} \\ \tau_2^{31} \\ \tau_2^{32} \\ \tau_2^{33} \\ \tau_2^{41} \\ \tau_2^{42} \\ \tau_2^{43} \\ \tau_2^{14} \\ \tau_2^{15} \\ \tau_2^{16} \\ \tau_2^{17} \\ \tau_2^{18} \\ \tau_2^{19} \\ \tau_2^{20} \\ \tau_2^{21} \\ \tau_2^{22} \\ \tau_2^{23} \\ \tau_2^{24} \\ \tau_2^{25} \\ \tau_2^{26} \\ \tau_2^{27} \\ \tau_2^{28} \\ \tau_2^{29} \\ \tau_2^{30} \end{bmatrix} = \begin{bmatrix} \tau^{13} \\ \tau^{14} \\ \tau^{15} \\ \tau^{16} \\ \tau^{17} \\ \tau^{18} \\ \tau^{19} \\ \tau^{20} \\ \tau^{21} \\ \tau^{22} \\ \tau^{23} \\ \tau^{24} \end{bmatrix} = \frac{1}{3\sqrt{2}} \begin{bmatrix} -1 & 2 & -1 & 1 & -2 & 1 \\ 2 & -1 & -1 & 1 & 1 & -2 \\ -1 & -1 & 2 & -2 & 1 & 1 \\ -1 & 2 & -1 & -1 & -2 & -1 \\ -1 & -1 & 2 & 2 & 1 & -1 \\ 2 & -1 & -1 & -1 & 1 & 2 \\ -1 & -1 & 2 & 2 & -1 & 1 \\ 2 & -1 & -1 & -1 & -1 & -2 \\ -1 & 2 & -1 & -1 & 2 & 1 \\ 2 & -1 & -1 & 1 & -1 & 2 \\ -1 & 2 & -1 & 1 & 2 & -1 \\ -1 & -1 & 2 & -2 & -1 & -1 \end{bmatrix} \begin{bmatrix} \sigma_{11} \\ \sigma_{22} \\ \sigma_{33} \\ \sigma_{12} \\ \sigma_{31} \\ \sigma_{23} \end{bmatrix} \quad (\text{A5.4})$$

and the stresses in the cube slip systems similar to $[001][011]$ are

$$\begin{bmatrix} \tau_3^{11} \\ \tau_3^{12} \\ \tau_3^{21} \\ \tau_3^{22} \\ \tau_3^{31} \\ \tau_3^{32} \end{bmatrix} = \begin{bmatrix} \tau^{25} \\ \tau^{26} \\ \tau^{27} \\ \tau^{28} \\ \tau^{29} \\ \tau^{30} \end{bmatrix} = \frac{1}{\sqrt{2}} \begin{bmatrix} 0 & 0 & 0 & 1 & 1 & 0 \\ 0 & 0 & 0 & 1 & -1 & 0 \\ 0 & 0 & 0 & 1 & 0 & 1 \\ 0 & 0 & 0 & 1 & 0 & -1 \\ 0 & 0 & 0 & 0 & 1 & 1 \\ 0 & 0 & 0 & 0 & 1 & -1 \end{bmatrix} \begin{bmatrix} \sigma_{11} \\ \sigma_{22} \\ \sigma_{33} \\ \sigma_{12} \\ \sigma_{31} \\ \sigma_{23} \end{bmatrix} \quad (\text{A5.5})$$

The final step is to develop a correlation between stress in the slip direction, τ , and the stresses τ_1 , τ_2 , and τ_3 that control the core width of a partial dislocation in the octahedral slip system. Consider, for example, the stresses in the $[111][10\bar{1}]$ slip system. Recall that τ_1 is normal to τ in the slip plane, thus τ_1 can be identified as τ_{13} . The stress τ_2 is parallel to τ_1 or $[10\bar{1}]$ on an intersection cube plane, thus τ_2 is τ_{28} . The stress τ_3 is normal to τ in the intersecting octahedral plane; thus τ_3 is τ_{16} . The same approach is used to determine the remaining correlations given in Table A-3.

Table A-3. Correlation Among the 12 Shear Stresses τ in the Octahedral Slip System and the Stress Components τ_1 , τ_2 , and τ_3 That Control the Core Width of a Partial Dislocation.

τ	τ_1	τ_2	τ_3
1	13	28	16
2	14	26	20
3	15	30	24
4	16	28	13
5	17	29	19
6	18	25	22
7	19	29	17
8	20	26	14
9	21	27	23
10	22	25	18
11	23	27	21
12	24	30	15

The inelastic strain in the principal coordinates of the material will be developed next from the slip in each of the slip systems. The local slip is equivalent to the local engineering shear strain. Let γ represent the local engineering shear strain in the right hand coordinate system defined by the unit normal vector n , the unit slip direction vector, p , and $s = n \times p$ where s is the vector parallel to the slip systems similar to $[111][112]$. Applying the second order tensor transformation rule gives the global tensor strain as a function of the local slip in the form

$$[\varepsilon] = \frac{1}{2} \lambda \begin{bmatrix} n_1 & n_2 & n_3 \\ p_1 & p_2 & p_3 \\ s_1 & s_2 & s_3 \end{bmatrix}^T \begin{bmatrix} 0 & 1 & 0 \\ 1 & 0 & 0 \\ 0 & 0 & 0 \end{bmatrix} \begin{bmatrix} n_1 & n_2 & n_3 \\ p_1 & p_2 & p_3 \\ s_1 & s_2 & s_3 \end{bmatrix} \quad (\text{A5.6})$$

Calculation of the inelastic strain, $\varepsilon_{ij}^{\text{II}}$, in the principal coordinates of the material due to the slip in the 12 primary octahedral slip directions gives

$$\begin{aligned} \frac{12}{\sqrt{6}} \begin{bmatrix} \varepsilon_{11}^{\text{II}} & \varepsilon_{12}^{\text{II}} & \varepsilon_{13}^{\text{II}} \\ \varepsilon_{21}^{\text{II}} & \varepsilon_{22}^{\text{II}} & \varepsilon_{23}^{\text{II}} \\ \varepsilon_{31}^{\text{II}} & \varepsilon_{32}^{\text{II}} & \varepsilon_{33}^{\text{II}} \end{bmatrix} &= \gamma_{11}^1 \begin{bmatrix} 2 & 1 & 0 \\ 1 & 0 & -1 \\ 0 & -1 & -2 \end{bmatrix} + \gamma_{12}^1 \begin{bmatrix} 0 & -1 & 1 \\ -1 & -2 & 0 \\ 1 & 0 & 2 \end{bmatrix} + \gamma_{13}^1 \begin{bmatrix} 2 & 0 & 1 \\ 0 & -2 & 1 \\ 1 & -1 & 0 \end{bmatrix} \\ &+ \gamma_{21}^1 \begin{bmatrix} -2 & 1 & 0 \\ 1 & 0 & -1 \\ 0 & -1 & 2 \end{bmatrix} + \gamma_{22}^1 \begin{bmatrix} -2 & 0 & -1 \\ 0 & -2 & -1 \\ -1 & -1 & 0 \end{bmatrix} + \gamma_{23}^1 \begin{bmatrix} 0 & -1 & -1 \\ -1 & 2 & 0 \\ -1 & 0 & -2 \end{bmatrix} \\ &+ \gamma_{31}^1 \begin{bmatrix} 2 & 0 & -1 \\ 0 & -2 & -1 \\ -1 & -1 & 0 \end{bmatrix} + \gamma_{32}^1 \begin{bmatrix} 0 & -1 & 1 \\ -1 & 2 & 0 \\ 1 & 0 & -2 \end{bmatrix} + \gamma_{33}^1 \begin{bmatrix} 2 & -1 & 0 \\ -1 & 0 & -1 \\ 0 & -1 & -2 \end{bmatrix} \\ &+ \gamma_{41}^1 \begin{bmatrix} 0 & -1 & -1 \\ -1 & -2 & 0 \\ -1 & 0 & 2 \end{bmatrix} + \gamma_{42}^1 \begin{bmatrix} -2 & -1 & 0 \\ -1 & 0 & -1 \\ 0 & -1 & 2 \end{bmatrix} + \gamma_{43}^1 \begin{bmatrix} -2 & 0 & 1 \\ 0 & 2 & -1 \\ 1 & -1 & 0 \end{bmatrix} \end{aligned} \quad (\text{A5.7})$$

and the strain in the secondary octahedral [111][112] are given by

$$\begin{aligned} \frac{12}{\sqrt{6}} \begin{bmatrix} \varepsilon_{11}^{\text{I2}} & \varepsilon_{12}^{\text{I2}} & \varepsilon_{13}^{\text{I2}} \\ \varepsilon_{21}^{\text{I2}} & \varepsilon_{22}^{\text{I2}} & \varepsilon_{23}^{\text{I2}} \\ \varepsilon_{31}^{\text{I2}} & \varepsilon_{32}^{\text{I2}} & \varepsilon_{33}^{\text{I2}} \end{bmatrix} &= \gamma_{11}^2 \begin{bmatrix} -2 & 1 & -2 \\ 1 & 4 & 1 \\ -2 & 1 & -2 \end{bmatrix} + \gamma_{12}^2 \begin{bmatrix} 4 & 1 & 1 \\ 1 & -2 & -2 \\ 1 & -2 & -2 \end{bmatrix} + \gamma_{13}^2 \begin{bmatrix} -2 & -2 & 1 \\ -2 & -2 & 1 \\ 1 & 1 & 4 \end{bmatrix} \\ &+ \gamma_{21}^2 \begin{bmatrix} -2 & -1 & -2 \\ -1 & 4 & -1 \\ -2 & -1 & -2 \end{bmatrix} + \gamma_{22}^2 \begin{bmatrix} -2 & -2 & 1 \\ 1 & -2 & -1 \\ 1 & -1 & 4 \end{bmatrix} + \gamma_{23}^2 \begin{bmatrix} 4 & -1 & 1 \\ -1 & 2 & 2 \\ 1 & 2 & -2 \end{bmatrix} \\ &+ \gamma_{31}^2 \begin{bmatrix} -2 & 2 & -1 \\ 2 & -2 & 1 \\ -1 & 1 & 4 \end{bmatrix} + \gamma_{32}^2 \begin{bmatrix} 4 & -1 & -1 \\ -1 & 2 & -2 \\ -1 & -2 & -2 \end{bmatrix} + \gamma_{33}^2 \begin{bmatrix} -2 & -1 & 2 \\ -1 & 4 & 1 \\ 2 & 1 & -2 \end{bmatrix} \\ &+ \gamma_{41}^2 \begin{bmatrix} 4 & 1 & -1 \\ -1 & -2 & 2 \\ -1 & 2 & -2 \end{bmatrix} + \gamma_{42}^2 \begin{bmatrix} -2 & 1 & 2 \\ 1 & 4 & -1 \\ 2 & -1 & -2 \end{bmatrix} + \gamma_{43}^2 \begin{bmatrix} -2 & -2 & -1 \\ -2 & -2 & -1 \\ -1 & -1 & 4 \end{bmatrix} \end{aligned} \quad (\text{A5.8})$$

The strain, ϵ_{ij}^{I3} , for the cube slip system can be written as

$$\begin{aligned} \frac{4}{\sqrt{2}} \begin{bmatrix} \epsilon_{11}^{I3} & \epsilon_{12}^{I3} & \epsilon_{13}^{I3} \\ \epsilon_{21}^{I3} & \epsilon_{22}^{I3} & \epsilon_{23}^{I3} \\ \epsilon_{31}^{I3} & \epsilon_{32}^{I3} & \epsilon_{33}^{I3} \end{bmatrix} &= \gamma_{11}^3 \begin{bmatrix} 0 & 1 & 1 \\ 1 & 0 & 0 \\ 1 & 0 & 0 \end{bmatrix} + \gamma_{12}^3 \begin{bmatrix} 0 & 1 & -1 \\ 1 & 0 & 0 \\ -1 & 0 & 0 \end{bmatrix} + \gamma_{21}^3 \begin{bmatrix} 0 & 1 & 0 \\ 1 & 0 & 1 \\ 0 & 1 & 0 \end{bmatrix} \\ &+ \gamma_{22}^3 \begin{bmatrix} 0 & 1 & 0 \\ 1 & 0 & -1 \\ 0 & -1 & 0 \end{bmatrix} + \gamma_{31}^3 \begin{bmatrix} 0 & 0 & 1 \\ 0 & 0 & 1 \\ 1 & 1 & 0 \end{bmatrix} + \gamma_{32}^3 \begin{bmatrix} 0 & 0 & -1 \\ 0 & 0 & 1 \\ -1 & 1 & 0 \end{bmatrix} \end{aligned} \quad (A5.9)$$

As a check of the calculations, notice that the inelastic strains given by Equations A5.7 to A5.9 are symmetric.

A.6 MODELING OF SINGLE CRYSTAL ALLOYS

The next step in the process is to develop a constitutive model to relate the slip on the slip plane to the shear stress on the slip plane in the slip direction following the methods developed by Sheh and Stouffer, 1988 and 1990. Let us begin by reviewing the ideas that will be used to develop a model:

Only octahedral slip is observed at temperatures below the critical temperature, about 700°C, for high strain rate loading. At temperatures above the critical temperature, deformation occurs by both octahedral and cube slip. Cube slip dominates near the [111] orientation and octahedral slip dominates near the [001] and [011] orientations.

Slip, or plastic flow, occurs when the shear stress on the slip plane in the slip direction, τ , exceeds the critical shear stress. The tension-compression anisotropy occurs because the stresses normal to the slip direction on the slip plane and intersecting slip plane, τ_1 and τ_2 respectively, extend and contract the core width of partial dislocations. Small core widths increase the potential for cross slip. The shear stress on the cube plane parallel to an active slip system, τ_3 , also promotes cross slip at higher temperatures.

The small strain tensile response show the presence of strain recovery, thus a back stress variable should be included as part of the model. The variation in recovery with orientation shows that the effect of back stress will be different in the octahedral and cube slip systems.

The flat tensile curves show that there must be a balance between strain hardening and dynamic recovery. The strain rate sensitivity occurs from a change in the balance between the hardening rate and recovery rate.

The cyclic hardening suggests the need for a drag stress variable to model cyclic hardening that is different from strain hardening. However, note that some two-phase superalloys are nearly stable in cyclic testing, so only the initial value of the drag stress may be required.

Crystal lattice rotation occurs above a few percent strain in single slip system orientations. Crystal lattice rotation effects are expected to be present in tensile and creep response beyond 3 to 5% strain.

The inelastic or plastic strain or strain rate is obtained by summing the slip or slip rate of the individual slip systems. The strain in the principal coordinate of the material for the octahedral and cube slip systems is given in Section A.5.

The constitutive model is based on a unified strain approach where the total strain is decomposed into elastic, inelastic and thermal components. The coordinate system is assumed to be the principal coordinates of the material. For fcc crystals the principal directions are along the cubic edges or in the [100], [010] and [001] directions. Thus the load or strain in a structure must first be transformed to the principal coordinates of the material before using the equations developed in this section. The elastic strain in the principal directions is given by Equation A2.1. Recall for cubic symmetry that the elastic modulus, shear modulus and Poisson's ratio are independent. A method for determining the elastic constants was presented in Section A.2. The thermal strain in the principal coordinate system is isotropic; therefore the thermal strain components can be determined from the coefficient of thermal expansion. Equations A5.7, A5.8, and A5.9 can be used to determine the total inelastic strain rate as

$$\dot{\epsilon}_{ij}^I = \dot{\epsilon}_{ij}^{I1} + \dot{\epsilon}_{ij}^{I2} + \dot{\epsilon}_{ij}^{I3} \quad (\text{A6.1})$$

for the octahedral and cube slip systems acting simultaneously. This approach will require three separate flow equations, one for each type of slip system. Recall that partial dislocations are present in octahedral slip but not in cube slip. The parameters must be determined such that the correct flow equation will be operative under the correct conditions as summarized above. The accumulated inelastic strain is determined by integrating the inelastic strain rate. The modeling task therefore reduces to determining the flow equations for the octahedral and cube slip systems, incorporating the tension-compression asymmetry, and evaluating the material parameters.

Several of the polycrystalline materials have rather similar chemical compositions to the γ - γ' alloys and exhibit many similar time dependent features. Thus it is reasonable to use the same type of equation for the slip rate in the octahedral and cube slip systems. However, recall that the stresses in all three-slip systems will be required to model the core width effect. Defining the following indicial notation for the three slip systems:

$k = 1$ defines slip systems similar to [111][101] and $\alpha = 1, 4$ and $\beta = 1, 3$

$k = 2$ defines slip systems similar to [111][112] and $\alpha = 1, 4$ and $\beta = 1, 3$

$k = 3$ defines slip systems similar to [001][011] and $\alpha = 1, 3$ and $\beta = 1, 2$

Defining the inelastic flow equation in the above notation gives

$$\dot{\gamma}_{\alpha\beta}^{Ik} = D_k \exp \left[-A_k \left(\frac{Z_k^{\alpha\beta}}{|\tau_k^{\alpha\beta} - \Omega_k^{\alpha\beta}|} \right)^{n_{kl}} \right] \frac{\tau_k^{\alpha\beta} - \Omega_k^{\alpha\beta}}{|\tau_k^{\alpha\beta} - \Omega_k^{\alpha\beta}|} \quad (\text{A6.2})$$

where $Z_k^{\alpha\beta}$ and $\Omega_k^{\alpha\beta}$ are the drag stress and back stress, respectively, that are associated with the slip rate in each of the slip systems. The shear stresses in the active slip systems are denoted by $\tau_k^{\alpha\beta}$, and the difference between the shear stress and back stress, $\tau_k^{\alpha\beta} - \Omega_k^{\alpha\beta}$, is the

net stress required to produce slip. The parameters D_k and A_k are scale factors that will be used to separate the high and low strain rate response, and n_{k1} controls the strain rate sensitivity.

The back stress evolution equations discussed in appendix C included strain hardening and dynamic recovery terms. Sheh (1988) found a back stress model that satisfied the saturation condition and was more flexible than those in appendix C for modeling the response of the three types of slip systems. Writing his result in the above notation gives

$$\dot{\Omega}_k^{\alpha\beta} = F_k \left| \dot{\gamma}_k^{\alpha\beta} \right|^{n_{k3}} \left[\text{sign} \left(\dot{\gamma}_k^{\alpha\beta} \right) - \frac{\Omega_k^{\alpha\beta}}{\Omega_k^{\text{sat}}} \right] + G_k \left(\frac{\tau_k^{\alpha\beta}}{\tau_o} \right)^{n_{k2}} \tau_k^{\alpha\beta} \quad (\text{A6.3})$$

where F_k , G_k , n_{k2} , n_{k3} and Ω_k^{sat} are material parameters. The inelastic recovery is primarily modeled by the strain rate term. If the G_k term is small relative to the F_k term, the changes in the value of the back stress will be small during elastic loading and unloading. If there is a large change in the back stress during the inelastic strain recovery, then contribution of the second term is relatively small in the [001] orientation. The exponents in Equation A6.3 give more flexibility to model the amount of recovery. The parameter $\tau_o = 1$ MPa or KSI is included to normalize units of stress. The saturated back stress, Ω_k^{sat} , is assumed to be a constant for tensile and cyclic loading.

The drag stress is used to model the initial hardness through Z_o and the growth in hardness through an exponential evolution equation. Drag stress was chosen to modify the tension compression anisotropy because the yield stress is a measure of the initial resistance to slip. Using the slip system notation the cyclic growth in drag stress can be rewritten as

$$H_k^{\alpha\beta} = H_{k2} - (H_{k1} - H_{k2}) \exp \left(-m_k W_k^{\alpha\beta} \right) \quad (\text{A6.4})$$

where $W_k^{\alpha\beta} = \int \tau_k^{\alpha\beta} d\gamma_k^{\alpha\beta}$, is the accumulated inelastic work in each slip system. The parameters H_{k1} and H_{k2} are the initial and saturated values of the drag stress, respectively. Equation A6.4 is a measure of the resistance to slip in each slip system due to the initial hardness and the development of a dislocation network. Since the tension-compression asymmetry occurs in the slip systems similar to [111][101], only the $H_1^{\alpha\beta}$ needs to be modified. The simplest approach is to assume a linear relation between $Z_1^{\alpha\beta}$ and $\tau_1^{\alpha\beta}$, $\tau_2^{\alpha\beta}$, and $\tau_3^{\alpha\beta}$, i.e., let

$$Z_1^{\alpha\beta} = H_1^{\alpha\beta} + V_1 \tau_1^{\alpha\beta} + V_2 \left| \tau_2^{\alpha\beta} \right| + V_3 \tau_3^{\alpha\beta} \quad (\text{A6.5})$$

The material parameters V_1 , V_2 and V_3 must be determined to give the required asymmetry. From their definitions, $\tau_1^{\alpha\beta}$ and $\tau_3^{\alpha\beta}$ are defined to extend or constrict the core width and the ability of the dislocation to cross slip from the octahedral to cube plane. Thus when $\tau_1^{\alpha\beta}$ and $\tau_3^{\alpha\beta}$ are positive the resistance to slip, $Z_1^{\alpha\beta}$, is increased, but the resistance to slip is decreased

when $\tau_1^{\alpha\beta}$ and $\tau_3^{\alpha\beta}$ are negative. Thus the resistance to inelastic flow depends on both the magnitude and sign of $\tau_1^{\alpha\beta}$ and $\tau_3^{\alpha\beta}$. Recalling that $\tau_2^{\alpha\beta}$ is the thermally aided contribution of the cross slip, and the sign of $\tau_2^{\alpha\beta}$ is not relevant since the potential to cross slip is the same in tension and compression. The parameters V_1 , V_2 and V_3 become less important with increasing temperature above the critical temperature. At very high temperatures $Z_1^{\alpha\beta} \rightarrow H_1^{\alpha\beta}$ and the orientation dependence disappears. The stresses $\tau_1^{\alpha\beta}$, $\tau_2^{\alpha\beta}$ and $\tau_3^{\alpha\beta}$ are defined in Table A-3.

A.7 MATERIAL PARAMETERS AND CALCULATED RESULTS

The following general assumptions and limitations are made to guide the development of the material parameters:

- The material constants are determined under isothermal conditions. Extension to thermomechanical response has not been attempted for single crystal alloys.
- The material parameter evaluation procedure is for strain rate controlled tensile and cyclic data.
- Single crystal response depends on strain rate and temperature. At high strain rate below about 600°C deformation occurs in the 12 slip systems similar to [111][101], between about 600°C and 850°C deformation occurs simultaneously by octahedral slip and cube slip (6 slip systems similar to [001][011]), and above 850°C orientation dependence becomes negligible.
- The octahedral slip constants are determined for tests where there is no cube slip. For example, data from tests in the [001] and [011] orientations can be used at any temperature to determine the octahedral constants. Conversely, the cube slip constants were determined from tests in the [111] orientation. The local stresses are given in Table A-1 for a 1000 pound tensile load in the [001], [011], and [111] orientations.

Table A-1 shows that tensile loading in the [001] orientation will produce equal slip rates in eight slip systems. The shear stress in the slip plane producing slip is 0.408 of the applied tensile load. Likewise, there are assumed to be eight equal slip rates, $\dot{\gamma}$, that add up to the inelastic strain rate, $\dot{\epsilon}^I$, in the [001] orientation. The slip system indices are dropped since there are eight equal shear stresses and slip rates in the [001] orientation. In this case Equation A5.7 can be used to show that $\dot{\gamma} = (12/16\sqrt{6})\dot{\epsilon}^I = 0.306\dot{\epsilon}^I$ after noting that stresses corresponding to the $\dot{\gamma}_{21}^I$, $\dot{\gamma}_{22}^I$, $\dot{\gamma}_{42}^I$ and $\dot{\gamma}_{43}^I$ slip systems are negative (see Table A-1). Similar results can be established for the [011] (or [111]) orientation since there are four (or three) equal shear stresses and slip rates. Thus, the local shear stresses and local slip rates for tensile, cyclic and creep tests in the [001], [011] and [111] orientations can be obtained from experimental data.

Since the equations are the same in both octahedral and cube slip systems, the discussion of determining parameters will be limited to the octahedral system as an example. This system includes the tension-compression asymmetry terms. The method of determining parameters is divided into the following three sequential steps for the evaluation of the:

- flow equation parameters
- back stress parameters
- drag stress parameters.

The order of the steps must be preserved since the information flow is sequential.

In the flow Equation A6.2 the parameter D_0 is a somewhat arbitrary scale factor that correlates with the maximum inelastic strain rate. Typically it is a factor 10^4 sec.^{-1} greater than the maximum expected strain rate in a particular application. For example, $D_0 = 1 \text{ sec.}^{-1}$ for creep, $D_0 = 10^4 \text{ sec.}^{-1}$ for tensile and fatigue response for strain rates up to 1.0 sec.^{-1} , and $D_0 = 10^6 \text{ sec.}^{-1}$ or greater for wave propagation and high rate loading applications.

Since n controls the strain rate sensitivity, let us begin with the parameters in the flow equation and experimental tensile response data. At tensile data saturation, (the strain at which the stress-strain curve becomes flat) the inelastic strain rate is equal to the total strain rate, $\dot{\epsilon}_o^I$, which is constant in a constant strain rate tensile test. At saturation the back stress is at the maximum value, Ω_m and the drag stress is near the initial value Z_o and remains almost constant. Thus for saturated, isothermal, tensile loading Equation A6.2 becomes

$$\dot{\gamma}_{1s}^I = D_1 \exp \left[-A_1 \left(\frac{Z_{1o}}{|\tau_{1s} - \Omega_{1m}|} \right)^{n_{11}} \right] \quad (\text{A7.1})$$

without the slip system numbers since they are all equal. The last term, $\tau - \Omega/|\tau - \Omega|$, in Equation A7.1 is equal to plus one. Using this result, Equation A6.2 can be inverted and written in the form

$$X^{1/n_{11}} = \left[-\frac{1}{A_1} \ln \left(\frac{\dot{\gamma}_{1s}^I}{D_1} \right) \right]^{1/n_{11}} = \frac{Z_{1o}}{\tau_s - \Omega_{1m}} \quad (\text{A7.2})$$

which can be used to find n , Ω_m and Z_o assuming that D_1 is assigned a value as described above. Equation A6.5 can be rewritten as

$$\tau_s X_s^{1/2n} = H_{11} + V_1 \tau_{1s} + V_2 |\tau_{2s}| + V_3 \tau_{3s} + \Omega_s X_s \quad (\text{A7.3})$$

after using Equation A6.4 in Equation A7.2 with $k = 1$. Recall the initial value of the drag stress in the octahedral slip system is H_{11} , and Ω_s is one of the eight equal values of the saturated back stress in the [001] orientation. Assuming a value for n_{11} (the strain rate sensitivity exponent), Equation A7.3 becomes a linear equation with five unknown parameters, H_{11} , V_1 , V_2 , V_3 , and Ω_s . At least five sets of data pairs ($X_s^{1/2n}$, τ_s) are required to evaluate these parameters in a least squares routine. These data can come from tension and compression tests at different strain rates in the [001] and [011] orientations. An iteration procedure can be used to determine the parameters. To summarize, start by assuming a value for n_{11}

($0.1 > n_{11} > 3.0$) and calculate H_{11} , V_1 , V_2 , V_3 , and Ω_{sat} from the data. Iterate until the saturated back stress falls in an acceptable range as described next.

The maximum value of the back stress can vary widely in different types of materials. The value during tensile loading must be positive (opposite to the tensile stress) and less than the saturated tensile stress, that is $0 \leq \Omega_m \leq \sigma_s$. In an extensively warm worked material that has developed subgrains and raised the yield strength considerably, the back stress is quite small when compared to the drag stress (Miller, 1975). In undeformed large grain materials the maximum value of the back stress can easily be greater than one half of the saturated tensile stress. Milligan and Antolovich (1989) determined values for the saturated back stress as large as $0.85\sigma_s$ in PWA 1480, a single crystal alloy with large precipitates. Large values of back stress are also verified by cyclic loading if reverse plastic flow begins before the applied stress reaches zero on unloading. To summarize, the following assumptions can be use if no other data is available:

$$\begin{aligned}\Omega_m &\approx 0.0 \text{ to } 0.3\sigma_s && \text{for small grain materials} \\ \Omega_m &\approx 0.5 \text{ to } 0.7\sigma_s && \text{for large grain materials}\end{aligned}\tag{A7.4}$$

It is very difficult to determine Ω_m from only tensile data; therefore it may be necessary to use an approximation. If cyclic data is available then other methods can be used to determine Ω_m .

The parameters in the back stress equation will be determined next. If only tensile data is available it is reasonable to assume the maximum value of the back stress can be approximated by Equation A7.4, and the values of Z_0 and n have been determined as described above. In this case a back stress history can be determined from the tensile data by using the inverted flow equation, Equation A7.2. The back stress history can then be used to determine the back stress rate as a function of time,

$$\Omega(t) = \tau(t) - \frac{1}{X^{1/2n}(t)} [H_{11} + V_1\tau_1(t) + V_2|\tau_2(t)| + V_3\tau_3(t)]\tag{A7.5}$$

The back stress rate can be obtained by numerical differentiation of the back stress history. This is reasonable for a computer acquired data file with hundreds of data points, but it not easy for hand digitized data.

The constants G_1 and n_{12} in the back stress Equation A6.3 can be determined from the initial value of the back stress rate during the initial "elastic" loading phase of the tensile history. Since the initial back stress rate is proportional to the stress rate or strain rate,

$$\dot{\Omega}_1(0) = G_1 \left(\frac{\tau_1}{\tau_o} \right)^{n_{12}} \dot{\tau}_1(0)\tag{A7.6}$$

the initial value of the back stress rate can be correlated to the local stress rate. The parameters G_1 and n_{12} are determined from the log linear slope of the line. The parameters n_{13} and F_1 for the inelastic term can be determined from the back stress rate in a tensile test.

The back stress rate is then determined numerically using the post yield uniaxial test data. Rearranging the Equation A7.5 for $k = 1$ and $\tau_0 = 1$ MPa or KSI gives

$$\frac{\left[\dot{\Omega} - G_1(\tau)^{n_{k2}} \dot{\tau} \right]}{\left[1 - \frac{\Omega}{\Omega_{\text{lsat}}} \right]} = F_1 |\dot{\gamma}|^{n_{13}} \quad (\text{A7.7})$$

The equation can be used with tensile data and/or recovery to determine n_{13} and F_1 . A log-linear curve of the data can be used to determine the parameters n_{13} and F_1 .

The next step is to develop a method to evaluate the material parameters for the drag stress equation. First, recall that the parameters in the flow and back stress equations have been evaluated. The inverted flow Equation A7.3 can be solved for the drag stress history

$$H_1(t) = \tau X^{1/2n} - V_1 \tau_1 - V_2 |\tau_2| - V_3 \tau_3 - \Omega X \quad (\text{A7.8})$$

for log term tensile loading or cyclic loading. The parameter $X^{1/2n}$ is the mapped inelastic strain rate defined in Equation A7.2.

The parameter m_1 that controls the rate of hardening or softening can be estimated by estimating the total accumulated inelastic strain or work required to produce the cyclically stable response. As the material response approaches the long-term stable response the exponential function in Equation A6.4 must approach zero and $H_1(t) = H_{12}$. Assuming a stable response occurs when the drag stress is within one percent of saturation, Equation A6.4 becomes

$$\frac{H(t) - H_{12}}{Z_{11} - Z_{12}} = 0.01 = \exp(-m_1 W_1^I) \quad (\text{A7.9})$$

where W_1^I is the accumulated inelastic work required to reach the cyclically stable state. The value of m_1 can then be estimated from the accumulated inelastic work at saturation. The accumulated inelastic strain $|\epsilon^I|$ can be substituted for W^I to obtain a slightly different representation.

A. REFERENCES

- Dame, L.T. and Stouffer, D.C. (1985). Anisotropic constitutive model for nickel base single crystal alloys: model development and finite element implementations, *NASA CR-175015*.
- Dame, L.T., and Stouffer (1988). A crystallographic model for nickel base single crystal alloys, *Journal of Applied Mechanics*, Vol. 55, pp. 325–331.
- Hopgood A.A. and Martin J.W (1986), The Creep Behavior of a Nickel Based Crystal Superalloy, *Mat Sci Engr*, 82:27–36.
- Kear, H.B., G.R. Leverant and J.M. Objak (1969). An analysis of creep induced intrinsic/extrinsic fault pairs in a precipitation hardened nickel-base alloy, *Transactions American Society of Metals*, Vol. 62, pp. 639–650.
- Lall C., Chin S., and Pope D. (1979), The Orientation and Temperature Dependence of the Yield Stress of Ni3(Al, Nb) Single Crystals, *Metallurgical Transactions*, 10A:1323.
- Leverant, G.R. and H.B. Kear (1970). The mechanism of creep in a γ' precipitation hardened nickel-base superalloy at intermediate temperatures, *Metallurgical Transactions*, Vol. 1, pp. 491–498.
- Leverant, G.R., H.B. Kear and J.M. Objak (1973). Creep of precipitation hardened nickel-base superalloy single crystals at high temperature, *Metallurgical Transactions*, Vol. 4, pp. 355–362.
- MacKay, R.A. and R.D. Maier (1982), "The influence of Orientation on the Stress Rupture Properties of Nickel Base Superalloy Single Crystals", *Metallurgical Transactions* 13A, pp. 1747–1754.
- Milligan W.W., and Antolovich S.D. (1989) "Deformation Modeling and Constitutive Modeling of Anisotropic Superalloys", *NASA CR 4215*.
- Miner, R., Voigt, R., Gayda, J. and Gabb, T. (1986) "Orientation and Temperature Dependence of Some Mechanical Properties of the Nickel Base Single Crystal Alloy Rene N4: Part 1, Tensile Behavior", *Metallurgical Transactions*, 17A, p. 491.
- Miner, R., Voigt, R., Gayda, J. and Gabb, T. (1986) "Orientation and Temperature Dependence of Some Mechanical Properties of the Nickel Base Single Crystal Alloy Rene N4: Part 3, Tension/Compression Anisotropy", *Metallurgical Transactions*, 17A, p 507.
- Paidar, V., Pope, D.P., and Vitek, V. (1984) "A Theory of the Anomalous Yield Behavior in L12 Ordered Crystals", *Acta Metall* V23.3, pp. 435–448.
- Pollock T. and Argon A. (1991) "Creep Resistance of Superalloy Single Crystals: Experiments and Modeling", *Modeling the Deformation of Crystalline Solids*, Ed. T.C. Lowe, A.D. Rollet, P.S. Follansbee and G.S. Daehn, The Minerals, Metals and Materials Society.
- Sheh, M.Y., and Stouffer, D.C., (1988). Anisotropic constitutive modeling of nickel base single crystal superalloy, *NASA CR 182157*.
- Sheh, M.Y. and Stouffer, D.C., (1990). "A Crystallographic Model for Tensile and Fatigue Response of Rene' N4 at 982 °C, *ASME Journal of Applied Mechanics*, Vol. 57. pp. 25–31.

APPENDIX B - EVALUATION OF THE GVIPS CONSTITUTIVE MODEL AND COMPARE CODE

B.1 INTRODUCTION

Generalized Viscoplasticity models with a Potential Structure (GVIPS) have been developed to predict the mechanical response of high temperature materials with anisotropic and inelastic properties under complex thermomechanical loading environments, (Saleeb and Wilt, 1993, and Arnold and Saleeb, 1994). Further these models have been implemented in the computer code COMPARE to evaluate the material parameters from files of experimental data using nonlinear optimization techniques, (Saleeb et. al.). The purpose of the current study is to evaluate the possible application of the GVIPS model for the directionally solidified alloy R142 at high temperature.

B.2 THE GVIPS MODEL

The GVIPS model is comprised of coupled system of tensorial rate equations which give the evolution of the state variables as a function of the external loading. The flow equation for the inelastic strain rate $\dot{\underline{\epsilon}}^I$ is given by

$$\dot{\underline{\epsilon}}^I = \sum_1^5 \frac{\langle F^{n_j} \rangle}{2\mu_j} \underline{\Gamma} \quad (\text{B.2.1})$$

and the evolution law for the back stress state variable $\underline{\alpha}$ is given by

$$\dot{\underline{\alpha}} = \left[\underline{Z}_m + \frac{h'}{h(1+2\beta)} (\underline{\alpha} \otimes \underline{\alpha}) \right] : \left(h \dot{\underline{\epsilon}}^I - \underline{R}_\alpha G^m \underline{\Pi} \right) \quad (\text{B.2.2})$$

where $h = H/G^\beta$, $h' = -\beta H/G^{\beta+1}$ and $\underline{Z}_m = \underline{M}^{-1}$. The other parameters in the inelastic flow and back stress equations are given by

$$\underline{F} = \frac{1}{2\kappa_0^2} (\underline{\sigma} - \underline{\alpha}) : \underline{M} : (\underline{\sigma} - \underline{\alpha}) - 1 \quad (\text{B.2.3})$$

$$\underline{G} = \frac{1}{2\kappa_0^2} (\underline{\alpha}) : \underline{M} : (\underline{\alpha}) \quad (\text{B.2.4})$$

$$\underline{\Gamma} = \underline{M} : (\underline{\sigma} - \underline{\alpha}) \quad (\text{B.2.5})$$

$$\underline{\Pi} = \underline{M} : \underline{\alpha} \quad (\text{B.2.6})$$

$$\underline{M} = \underline{P} - \xi \underline{Q} - \frac{1}{2} \zeta \underline{R} \quad (\text{B.2.7})$$

In the application for R142 alloy the isotropic hardening parameter κ_0 is held constant. The anisotropy of the material is introduced through Equation B.2.7. The two parameters ξ and ζ are defined as

$$\xi = \frac{\eta^2 - 1}{\eta^2} \quad \text{with} \quad \eta = \frac{\kappa_l}{\kappa_t} \quad (\text{B.2.8})$$

and

$$\varsigma = \frac{4(\varpi^2 - 1)}{4\varpi^2 - 1} \quad \text{with} \quad \varpi = \frac{Y_l}{Y_t} \quad (\text{B.2.9})$$

In the above equations, the material parameters κ_l and κ_t are the longitudinal and transverse shear strengths and, Y_l and Y_t are the longitudinal and transverse strengths in tension. The fourth order tensors P, Q and R are defined as

$$\underline{P} = \underline{I} - \frac{1}{3}(\underline{\delta} \otimes \underline{\delta}) \quad \underline{I}_{ijkl} = \frac{1}{2}(\delta_{ik}\delta_{jl} + \delta_{jk}\delta_{il}) \quad (\text{B.2.10})$$

$$\underline{Q}_{ijkl} = \frac{1}{2}(D_{ij}\delta_{kl} + D_{il}\delta_{jk} + D_{jk}\delta_{il} + D_{jl}\delta_{ik}) - 2D_{ij}D_{kl} \quad (\text{B.2.11})$$

$$\underline{R} = 3(\underline{D} \otimes \underline{D}) - (\underline{D} \otimes \underline{\delta} + \underline{\delta} \otimes \underline{D}) + \frac{1}{3}(\underline{\delta} \otimes \underline{\delta}) \quad (\text{B.2.12})$$

The tensor D is used to define the principal direction of the material as a function of the direction cosines, and δ is Kronecker delta. The GVIPS model has nine material parameters (κ_o , n , μ , m , β , R , H , ξ and ζ ,) that must be determined for any application. The inelastic strain rate must be integrated and added to the elastic strain to find the total strain.

B.3 EVALUATION OF A UNIAXIAL GVIPS EQUATION

The first step in determining the uniaxial model is to evaluate the tensor M for loading parallel to the principal axis of the material. In this case the material behavior will be pseudo-isotropic and only the tensor P in Equation B.2.7 is required. Let A be a second order tensor that represents the three normal components of stress or strain. The relationship between a three dimensional physical space and a six dimensional mathematical space is the given as

$$\underline{A} = \begin{bmatrix} a_{11} & 0 & 0 \\ 0 & a_{22} & 0 \\ 0 & 0 & a_{33} \end{bmatrix} = [a_{11} \ a_{22} \ a_{33} \ 0 \ 0 \ 0] \quad (\text{B.3.1})$$

Loading along the principal axis of the material will give the six-dimensional vector as $\underline{D} = [1 \ 0 \ 0 \ 0 \ 0 \ 0]$ and the Kronecker delta vector is written as $\underline{\delta} = [1 \ 1 \ 1 \ 0 \ 0 \ 0]$, so the Equation B.2.10 becomes

$$\underline{M} = \underline{P} = \begin{bmatrix} 1 & 0 & 0 \\ 0 & 1 & 0 \\ 0 & 0 & 1 \end{bmatrix} - \frac{1}{3} \begin{bmatrix} 1 & 1 & 1 \\ 1 & 1 & 1 \\ 1 & 1 & 1 \end{bmatrix} = \frac{1}{3} \begin{bmatrix} 2 & -1 & -1 \\ -1 & 2 & -1 \\ -1 & -1 & 2 \end{bmatrix} \quad (\text{B.3.2})$$

after eliminating the higher order tensor components which are all equal to zero. Equation B.3.2 is the representation for an isotropic material. Finally note that Equation B.3.2 is singular, so $Z_m = M^{-1}$ in the back stress equation can not be evaluated. This appears to be a fundamental inconsistency in the potential function formulation. The authors make the assumption that

$$Z_m = M^{-1} = \begin{bmatrix} 1 & 0 & 0 \\ 0 & 1 & 0 \\ 0 & 0 & 1 \end{bmatrix} \quad (\text{B.3.3})$$

for use in three dimensional applications.

The next step is to use Equations B.3.2 in Equations B.2.3 to B.2.7 to obtain a model for uniaxial loading. In the case we assume the uniaxial stress produces a non-zero inelastic strain rate in the three coordinate directions. This implies that there are three non-zero back stress coordinates, but the symmetry of the loading implies that $\varepsilon_{22} = \varepsilon_{33} = -\varepsilon_{11}/2$ and

$\alpha_{22} = \alpha_{33} = -\alpha_{11}/2$. Define $\dot{\varepsilon}^I$, σ and α as the uniaxial values of the inelastic strain rate, stress and back stress, respectively, then the overstress vector becomes

$$[\underline{\sigma} - \underline{\alpha}] = [\sigma - \alpha, \quad -\alpha/2, \quad -\alpha/2] \quad (\text{B.3.4})$$

Equations B.2.5 and B.2.6 then become

$$\underline{\Gamma} = \frac{1}{3}(\sigma - 3\alpha/2) \begin{bmatrix} 2 \\ -1 \\ -1 \end{bmatrix} \quad \text{and} \quad \underline{\Pi} = -\frac{1}{3}(3\alpha/2) \begin{bmatrix} 2 \\ -1 \\ -1 \end{bmatrix} \quad (\text{B.3.5})$$

The scalar functions F and G in Equations B.2.3 and B.2.4, respectively, can be written as

$$F = \frac{1}{3\kappa_0^2}(\sigma - 3\alpha/2)^2 - 1 \quad (\text{B.3.6})$$

$$G = \frac{1}{3\kappa_0^2}(3\alpha/2)^2 \quad (\text{B.3.7})$$

The inelastic flow equation for uniaxial loading is now given as

$$\dot{\varepsilon}^I = \frac{1}{3\mu} \left\langle \frac{(\sigma - 3\alpha/2)^2}{3\kappa_0^2} - 1 \right\rangle^n (\sigma - 3\alpha/2) \quad (\text{B.3.8})$$

and the back stress equation can be rewritten as

$$\dot{\alpha} = \frac{1}{(1 + 2\beta)} \left(\frac{H}{G^\beta} \dot{\varepsilon}^I - \alpha R_\alpha G^m \right) \quad (\text{B.3.9})$$

after simplifying the results.

These equations have been implemented in a simple FORTRAN computer code and integrated using a generalized trapezoidal method with small time steps. The results match the results from COMPARE using constants that were determined by COMPARE. The test cases included

tensile loading at constant strain rate, creep under constant stress, and a complicated multiple step creep loading.

B.4 EVALUATION OF THE MATERIAL PARAMETERS

In order to understand the roll of the material parameters in the GVIPS constitutive model, the equations were evaluated under specific conditions. This produced another approach to evaluating several of the parameters and helped to generate a single set of parameters that could be used for both tensile and creep loading. This result also provides guidance in selecting the initial values used in the COMPARE code.

Saturation. Saturation is defined at the condition when the stress and inelastic strain rate become constant in tensile or creep loading. This corresponds to the minimum creep rate during creep loading or the ultimate tensile stress during constant strain rate loading. In both cases the back stress in Equation B.3.8 is constant and the back stress rate is zero. This condition can be used to simplify Equations B.3.8 and B.3.9.

Consider first the inelastic flow equation. Since the term in the $\langle \rangle$ brackets is much greater than zero at saturation, Equation C.3.8 can be approximated as

$$3\mu(3\kappa_o^2)\dot{\epsilon}_s^I = (\sigma_s - 3\alpha_s/2)^{2n+1} \quad (B.4.1)$$

where the subscript s corresponds the value of the corresponding variables at saturation. Define the following parameters

$$D_o = 3\mu(3\kappa_o^2) \quad \text{and} \quad p = \frac{1}{2n+1} \quad (B.4.2)$$

so the inelastic flow equation becomes

$$(D_o\dot{\epsilon}_s^I)^p = (\sigma_s - 3\alpha_s/2) \quad (B.4.3)$$

This can be written an a logarithmic linear representation in the form

$$p \log D_o + p \log \dot{\epsilon}_s^I = \log(\sigma_s - 3\alpha_s/2) \quad (B.4.4)$$

which can be solved for D_o and p using the method of least squares and the saturation data if the saturation values of the back stress are known.

The back stress evolution rate will be zero at saturation, thus Equation B.3.9 can be written as

$$\dot{\epsilon}_s^I = \frac{2}{3} \left(\frac{3}{2} \alpha_s \right) \left(\frac{R_\alpha}{H} \right) \left[\frac{1}{3\kappa_o^2} \left(\frac{3}{2} \alpha_s \right)^2 \right]^{\beta+m} \quad (B.4.5)$$

after using Equation B.3.7 and rearranging. Once again define two additional combinations of constitutive constants as

$$P_o = \frac{2}{3} \left(\frac{R_\alpha}{H} \right) \left(\frac{1}{3\kappa_o^2} \right)^{\beta+m} \quad \text{and} \quad q = 2(\beta+m)+1 \quad (B.4.6)$$

so the back stress equation at saturation can be rewritten as

$$\dot{\epsilon}_s^I = P_o \left(\frac{3}{2} \alpha_s \right)^q \quad (B.4.7)$$

Applying the method of least squares to Equation B.4.7 in the form

$$\log \dot{\epsilon}' = \log P_o + q \log (3\alpha_s/2) \quad (\text{B.4.8})$$

gives another linear representation that the creep and tensile saturation data must satisfy.

Back Stress History. Assume a strategy can be found to estimate the values of the back stress at saturation, α_s , so that D_o and p can be found from the saturation data. Defining

$X(t) = (D_o \dot{\epsilon}'(t))^p$ as a transformed value of the inelastic strain rate at any time in a deformation history, Equation B.4.3 can be solved for the back stress history

$$\alpha(t) = \frac{2}{3} [\sigma(t) - X(t)] \quad (\text{B.4.9})$$

upon using the stress and inelastic strain rate history from any test data file. The back-stress rate history, $\dot{\alpha}(t)$, can then be estimated by fitting a spline to the back stress history.

Rearranging Equation B.3.9 and using Equation B.4.6 gives

$$\frac{(1+2\beta)}{H} \left[\frac{1}{3\kappa_o^2} \left(\frac{3}{2} \alpha(t) \right) \right]^\beta \dot{\alpha}(t) = \dot{\epsilon}' - P_o \left(\frac{3}{2} \alpha(t) \right)^q \quad (\text{B.4.10})$$

which is another representation that the parameters must satisfy using data from a tensile or creep test. Define Q_o as

$$Q_o = (1+2\beta)/H \quad (\text{B.4.11})$$

and observe Equation C.4.10 can be written as

$$\log Q_o + \beta \log \left[\frac{1}{3\kappa_o^2} \left(\frac{3}{2} \alpha(t) \right) \right] = \log \dot{\epsilon}' - \log P_o \left(\frac{3}{2} \alpha(t) \right)^q - \log \dot{\alpha}(t) \quad (\text{B.4.12})$$

Equation B.4.12 can be solved for Q_o and β using the method of least squares after estimating a value for κ_o .

A Solution Strategy. At this point there are six parameter combinations (D_o , p , P_o , q , Q_o , β) to determine seven constitutive parameters (μ , κ_o , n , H , β , $R\alpha$, m) using the method of least squares. Further it is necessary to obtain an estimate for the saturated value of the back stress, α_s , before any of the equations can be used. The saturated value of the back stress is typically less than about 40% of the stress at saturation. The value of saturated back stress, α_s , physically corresponds to the balance between strain hardening and dynamic recovery, and depends on the grain size or mean distance between obstacles that pin dislocations. The back stress is usually negligible in alloys with very small grains, and near the upper limit for large grain alloys like R142. A good initial guess for R142 would be 30% to 35% of the saturated stress. Thus one approach is to estimate the value of α_s , and iterate on the estimate until the calculated values of the saturated stress and inelastic strain rates optimized. This method has been successfully used with other constitutive models, Stouffer and Dame, 1996.

A second approach was developed to estimate the saturated back stress as part of the effort to verify the above equations to evaluate the material parameters. In this case several R142 creep and tensile test files were loaded into the COMPARE code to determine the material

parameters. The parameters were then used in the uniaxial code to evaluate the back stress history. It was found that the saturated back stress, α_s , increases linearly from about 25% of the saturated creep stress to about 35% of the saturated back stress from the tensile tests. This saturated back stress model was used with the above equations to determine the material constants as described above. The calculated parameters were very close to the parameters determined from COMPARE, and the calculated model results were identical. This exercise confirms the above method to determine the parameters and provides insight into a method to model the saturated back stress for R142 at other temperatures.

Finally the calculated results were determined by assuming a small value for κ_0 . In a separate study it was shown that the calculated response is essentially the same for any small value of κ_0 . Thus κ_0 can almost be taken as a universal constant.

B.5 A MODEL FOR TERTIARY CREEP

In a separate study S. Arnold (1998) developed a model for tertiary creep that has been implemented into the uniaxial code and evaluated. The parameters in the model appear to have sufficient flexibility to model the tertiary creep of R142.

B.6 OVERALL EVALUATION OF THE GVIPS/COMPARE SYSTEM

In general, it was found that several changes had to be made to the COMPARE program to effectively use the program. These changes mainly embodied changing the user interface to facilitate entering experimental data so that multiple runs could be made without manually re-entering the data files. Once these changes had been made the program was much easier to run. However, COMPARE places several demands on the format of the experimental data. At first, these requirements were not understood since the code is still under development and a user manual was not available. These requirements include defining strain and time points at each point that a load change is made, and including the load up strains or stresses in the file (even though they are not always included in the measured data such as in a creep test). Once all the requirements were understood, it was relatively easy to run COMPARE and to generate meaningful results (and results that could be interpreted consistently with the uniaxial theory developed above).

Additionally, it should be remarked that the GVIPS theory is based on potential theory and not on metallurgical principals. As described in Appendix A, the single crystal theory relies heavily on such physical principals. It will be interesting to see how well the GVIPS approach will work on a total data set that incorporates several temperatures and several deformation mechanisms.

B. REFERENCES

Arnold, S.M. and Saleeb, A.F. (1994) "On the Thermodynamic Framework of Generalized Coupled Thermoelastic-Viscoplastic Damage Modeling", Int. Journal of Plasticity, V 10.3, pp 263–278.

Saleeb, A.F. and Wilt, T.E. (1993) "Analysis of the Anisotropic Viscoplastic Damage Response of Composite Laminates" Int. J Numerical Methods Eng. V.36, pp. 1629–1660.

Stouffer, D.L. and Dame, T.L. (1996). Inelastic deformation of metals: Models, mechanical properties, and metallurgy, John Wiley and Sons Inc., New York.

APPENDIX C - MODELING APPROACH

C.1 CHARACTERISTICS OF MODERN CONSTITUTIVE EQUATIONS

The state variable approach resulted from a synthesis of modeling, physical metallurgy and experimental results of many researchers and practitioners in the last two decades. The development was motivated by three general conclusions about the state of classical modeling. First, the yield surface approach to plasticity is not totally adequate. It is excellent for predicting the initial yield of metals, but the subsequent yield surfaces that evolve during a general multiaxial deformation history are not easy to model or experimentally quantify. The plastic strain increment vector is not always normal to the yield surface nor is it parallel to the deviatoric stress vector. Second, the addition of a creep strain to account for time effects is not fully adequate. The coupling between plastic and creep strain can be significant even in the traditional "constant stress" creep test where it is known that the initial loading rate effects the subsequent creep response. Time is not a good variable for constitutive modeling because it is not objective. Third, the results of physical metallurgy are largely ignored. An enormous body of fundamental knowledge about metals has been developed during the last half century. Information about the physical basis of deformation and the associated variables should be useful for modeling. Knowledge of the active deformation mechanism under different loading conditions will provide insight about the macroscopic response and clues for the choice of variables. A prior knowledge of the deformation mechanisms will guide experimental programs and the selection of materials for specific applications.

This section contains a discussion of the variables that are used in the state variable modeling and the structure of the equations that form the philosophy of the approach. The results from physical metallurgy and the classic approaches are examined to identify some specific choices for the state variables and the effect of these choices on the mathematical structure of the equations.

Characterizing the properties of dislocations and their reactions with grain boundaries, precipitates, and other dislocations could take many variables. Alternatively, implicit internal state variables are defined as macroscopic averages of events associated with the development of the microstructure. They characterize average properties associated with dislocation propagation, and their interaction with precipitates, grain boundaries, and other dislocations. In addition to the state variables there are external variables that are macroscopically defined or observed, and controlled, measured or calculated in an experimental program. These variables must be correlated with the internal state variables of the material during deformation.

Plastic and creep strain variables are not used. Instead a single, unified, inelastic strain variable is used to characterize all the inelastic effects. The kinematic equation used to determine the total strain tensor, ϵ^T , is the sum of the elastic, ϵ^E , inelastic, ϵ^I , and thermal strain tensors, ϵ^{TH} . Mathematically, the kinematic equation is represented by

$$\epsilon_{ij}^T = \epsilon_{ij}^E + \epsilon_{ij}^I + \epsilon_{ij}^{TH} \quad (C.1.1)$$

Equation C.1.1 avoids many of the issues associated with defining and characterizing plasticity separately and developing a rule for creep-fatigue interaction. The inelastic strain can be

uniquely determined experimentally from the total measured strain since the elastic and thermal strains are almost entirely unaffected by inelastic deformation. Time is avoided as a variable. Time dependent variables will be characterized by their rates such as the inelastic strain rate or state variable evolution rate. The inelastic strain rate, for example, can be integrated to obtain the accumulated inelastic strain at any point in the deformation history without ever using time explicitly as a state variable.

One objective of state variable constitutive modeling is to develop a correlation between the external variables and the internal state variables. The existence of this correlation permits the inelastic strain rate of a metal at any point in the deformation history to be determined from the current values of the external and internal variables. The inelastic strain rate at a later point in the history is determined by later values of the mechanical and thermal loads, and the later values of the state variables. Thus, the state variables must be continuously updated to account for the changes in the microstructure. The relationship between the current microstructure and previous deformation history is included in the model by updating the state variables; that is, the "history dependence", is included through the evolution of the state variables. The entire previous history of the deformation is characterized by the current state of the microstructure.

Mathematically, the state variable approach can be characterized by three types of equations: a kinematic equation, a kinetic equation, and a set of state variable evolution equations. The kinematic equation is used with the integral of the inelastic strain rate; that is,

$$\varepsilon_{ij}^T = \varepsilon_{ij}^E + \int_0^t \dot{\varepsilon}_{ij}^I d\tau + \varepsilon_{ij}^{TH} \quad (C.1.2)$$

where t is some time in the deformation history. The total strain and inelastic strain can be large or small, but the elastic strain is assumed to be small so a linear elastic stress-strain law can be used. The kinetic equation, or inelastic flow law, is formally written as

$$\dot{\varepsilon}_{ij}^I = \dot{\varepsilon}_{ij}^I(\sigma_{kl}, T, \zeta_k, \dots) \quad (C.1.3)$$

where $\dot{\varepsilon}_{ij}^I$ is the inelastic strain rate tensor that must be integrated with respect to time to obtain the accumulated inelastic strain. The stress, σ_{kl} , temperature, T , and other external and internal state variables ζ_k , are expected to be present. The state variables are used as macroscopic measures of the characteristics of the microstructure. The evolution equations to update the current values of the state variables are formally given as

$$\dot{\zeta}_k = \dot{\zeta}_k(\sigma_{ij}, \dot{\varepsilon}_{ij}^I, T, \zeta_i, \dots) \quad (C.1.4)$$

and must also be integrated with respect to time to determine their current values. At this point in the development the exact definition or number of state variables is undefined and needs to be established from the principles of physical metallurgy. Equations (C.1.2) to (C.1.4) establish the essential mathematical structure for all state variable models.

The next step is to identify some potential state variables. The state variables must be selected to describe the critical microstructural effects in anticipation that the predicted macroscopic

inelastic response will be accurate to a broad class of loading conditions and temperatures. Thus let us review the critical metallurgical and experimental observations that can be used to define the state variables and external variables. These important concepts are:

- a.) Inelastic deformation occurs at low temperature due to slip. The slip occurs on the slip planes closest to the planes with the maximum shear stress.
- b.) Inelastic deformation occurs at high temperature due to planar slip and dislocation climb, a diffusion controlled mechanism.
- c.) The accumulated inelastic strain does not produce a significant change in the inelastic volume.
- d.) The accumulated inelastic strain and strain rate appear to be independent of hydrostatic stress except for some alloys under extreme hydrostatic loading conditions.
- e.) Back stress (a resistance to slip) results from the interaction of dislocations with other dislocations, grain boundaries, precipitates, and other barriers. The net stress producing slip or inelastic strain is the over stress or the difference between the shear stress and back stress. The back stress is in the direction opposite to the local shear stress in uniaxial loading and is therefore expected to be orientation dependent in three dimensional loading.
- f.) The initial hardness of a metal is determined from the resistance to slip that is created by obstacles such as grain boundaries, precipitates, and interstitial atoms in the initial microstructure. These effects are isotropic and are modeled by the initial value of the drag stress.
- g.) Hardening is an increase in the resistance to deformation. It results primarily from the interaction of dislocations with other dislocations, precipitates and grain boundaries.
- h.) Dynamic recovery is the annihilation of dislocations during deformation that reduces the effective rate of hardening. It was shown that temperature and strain rate dependence results from the balance between the hardening and recovery rates.
- i.) Recovery is achieved by the formation of cells and subgrains. Cells and subgrains are orientation independent and monotonically approach a saturated state under uniform loading conditions.
- j.) Creep results primarily from the temperature dependent mechanisms of diffusion, dislocation glide, climb and rafting in single crystal superalloys. Creep in tension and compression are different due to the effect of lattice expansion or compression on the diffusion rate.
- k.) Static recovery results from the interaction stress between the dislocations themselves. The higher temperatures increase dislocation mobility and promote diffusion. Static recovery lowers the effective steady state hardening during creep. The rates of dynamic and static thermal recovery are much different.

The net effect of hardening and softening can be separated mathematically into two groups by their orientation dependent or orientation independent characteristics. This establishes the need for a minimum of two types of hardening state variables. A back stress tensor is introduced to model the hardening and recovery effects associated with the back stress effect. In addition, a scalar drag stress is used to model the development of hardening or softening associated with isotropic effects such as point defects, precipitates, cells and subgrains and grains. Other scalar state variables are introduced to model the net effect of hardening and static thermal recovery during creep. These variables will be introduced as necessary in the development of the different models.

The back stress effect has been incorporated in state variable models by many workers. In all cases, the kinetic equation for the inelastic strain rate, Equation C.1.3, has the form

$$\dot{\epsilon}_{ij}^I = \lambda (\sigma_{kl}, T, \zeta_k, \dots, S_{ij} - \Omega_{ij}) \quad (C.1.5)$$

where the deviatoric stress and deviatoric back stress are used to preserve the condition of no inelastic volume changes and the function λ depends on the other macroscopic and state variables. Equation (C.1.5) includes the effects of back stress by permitting reverse inelastic flow after unloading when the over stress, defined as the difference between the applied stress and the back stress, becomes negative. The tensorial property of the back stress also allows for orientation dependence that is consistent with the dislocation pile-ups discussed above. If the applied stress direction is changed, the direction of shear stress in the crystallographic slip system will also change, and slip would occur in another slip plane in a different direction producing different dislocation interactions. Thus the components of the back stress tensor will also change. Finally, the initial value of the back stress is usually assumed to be zero because dislocation interactions do not develop until after slip has started.

The drag stress variable, Z , is introduced to model the initial hardness, and the subsequent hardening or softening that develops during cycling. The initial value of drag stress, $Z(0) = Z_0$, is used to characterize the initial resistance to slip that is present in the undeformed microstructure. The evolution of the drag stress is associated with the interaction of dislocations with point (orientation independent) defects and the growth of cells and subgrains. Since the interaction of dislocations with precipitates, interstitial atoms, cells and subgrains is largely orientation independent, the drag stress is assumed to be a scalar. The drag stress is assumed to monotonically increase (for hardening) or decrease (for softening) to a saturated state in constant amplitude cycling.

REPORT DOCUMENTATION PAGE			Form Approved OMB No. 0704-0188	
Public reporting burden for this collection of information is estimated to average 1 hour per response, including the time for reviewing instructions, searching existing data sources, gathering and maintaining the data needed, and completing and reviewing the collection of information. Send comments regarding this burden estimate or any other aspect of this collection of information, including suggestions for reducing this burden, to Washington Headquarters Services, Directorate for Information Operations and Reports, 1215 Jefferson Davis Highway, Suite 1204, Arlington, VA 22202-4302, and to the Office of Management and Budget, Paperwork Reduction Project (0704-0188), Washington, DC 20503.				
1. AGENCY USE ONLY (Leave blank)		2. REPORT DATE May 2006		3. REPORT TYPE AND DATES COVERED Final Contractor Report
4. TITLE AND SUBTITLE Large Engine Technology (LET) Short Haul Civil Tiltrotor Contingency Power Materials Knowledge and Lifting Methodologies			5. FUNDING NUMBERS WBS-22-714-85-01 NAS3-26617	
6. AUTHOR(S) Samuel D. Spring				
7. PERFORMING ORGANIZATION NAME(S) AND ADDRESS(ES) GE Aircraft Engines 1000 Western Avenue Lynn, Massachusetts 01910			8. PERFORMING ORGANIZATION REPORT NUMBER E-14886	
9. SPONSORING/MONITORING AGENCY NAME(S) AND ADDRESS(ES) National Aeronautics and Space Administration Washington, DC 20546-0001			10. SPONSORING/MONITORING AGENCY REPORT NUMBER NASA CR-2006-213378	
11. SUPPLEMENTARY NOTES This research was originally published internally as AST036 in July 2000. Project Manager, Joseph Eisenberg (retired). Responsible person, Steven M. Arnold, Materials and Structures Division, NASA Glenn Research Center, organization code RXL, 216-433-3334.				
12a. DISTRIBUTION/AVAILABILITY STATEMENT Unclassified - Unlimited Subject Category: 39 Available electronically at http://gltrs.grc.nasa.gov This publication is available from the NASA Center for AeroSpace Information, 301-621-0390.			12b. DISTRIBUTION CODE	
13. ABSTRACT (Maximum 200 words) This report documents the results of an experimental program conducted on two advanced metallic alloy systems (René 142 directionally solidified alloy (DS) and René N6 single crystal alloy) and the characterization of two distinct internal state variable inelastic constitutive models. The long term objective of the study was to develop a computational life prediction methodology that can integrate the obtained material data. A specialized test matrix for characterizing advanced unified viscoplastic models was specified and conducted. This matrix included strain controlled tensile tests with intermittent relaxation test with 2 hr hold times, constant stress creep tests, stepped creep tests, mixed creep and plasticity tests, cyclic temperature creep tests and tests in which temperature overloads were present to simulate actual operation conditions for validation of the models. The selected internal state variable models were shown to be capable of representing the material behavior exhibited by the experimental results; however the program ended prior to final validation of the models.				
14. SUBJECT TERMS Engine design; Tiltrotor aircraft; Contingency			15. NUMBER OF PAGES 65	
			16. PRICE CODE	
17. SECURITY CLASSIFICATION OF REPORT Unclassified	18. SECURITY CLASSIFICATION OF THIS PAGE Unclassified	19. SECURITY CLASSIFICATION OF ABSTRACT Unclassified	20. LIMITATION OF ABSTRACT	

